Journal of Asian Earth Sciences 35 (2009) 554–570

Contents lists available at ScienceDirect

Journal of Asian Earth Sciences

journal homepage: www.elsevier.com/locate/jaes

Hf–Nd isotopic decoupling in continental mantle lithosphere beneath Northeast China: Effects of pervasive mantle metasomatism

Song-Yue Yu [a,b], Yi-Gang Xu [a,*], Xiao-Long Huang [a], Jin-Long Ma [a], Wen-Chun Ge [c], Hui-Huang Zhang [d], Xiu-Feng Qin [a]

[a] Key Laboratory of Isotope Geochronology and Geochemistry, Guangzhou Institute of Geochemistry, Chinese Academy of Sciences, Guangzhou 510640, China
[b] State Key Laboratory of Ore Deposit Geochemistry, Institute of Geochemistry, Chinese Academy of Sciences, Guiyang 550002, China
[c] College of Earth Sciences, Jilin University, Changchun 130061, China
[d] Institute of Geology and Geophysics, Chinese Academy of Sciences, Beijing 100029, China

ARTICLE INFO

Article history:
Received 21 March 2008
Received in revised form 5 April 2009
Accepted 23 April 2009

Keywords:
Peridotite xenoliths
Geochemistry
Hf–Nd isotopic decoupling
Chromatographic metasomatism
Lithospheric mantle
NE China

ABSTRACT

Nd–Hf isotopic decoupling has frequently been observed in the continental and oceanic mantle, but its origin remains controversial. Here we present combined elemental and Sr–Nd–Hf isotopic study on peridotite xenoliths entrained in Cenozoic basalts from Shuangliao and Jiaohe in Northeast China, which provides insight into this issue. The data reveal a heterogeneous lithospheric mantle beneath Northeastern China, consisting of fertile (type I) to strongly refractory (type II) peridotites. Type I peridotites are largely shielded from late metasomatism, thus preserving information of depletion events. Nd model age suggests a Proterozoic lithospheric mantle beneath NE China. Type II peridotites are mostly refractory harzburgites and show ubiquitous enrichment of incompatible elements. They are further divided into two sub-groups. Clinopyroxenes from type IIa samples have high and wide Lu/Hf (0.34–1.3) and very radiogenic Hf isotopic ratios (ε_{Hf} = 44.4–63.8). Hf concentration is generally low (0.12–0.43 ppm) and plots along or slightly above the modeled partial melting depletion trend. In contrast, Nd content in type IIa clinopyroxenes is significantly higher than the modeled concentrations in residues at a given degree of melt depletion. The difference in enrichment of Hf and Nd translates to decoupling of Lu/Hf–Sm/Nd ratios and of Nd–Hf isotopes (ε_{Nd} = −1.3 to 8.4). Clinopyroxenes from most of type IIb peridotites have relatively low Lu/Hf ratios (0.04–0.24) and coupled Nd–Hf isotopes. Both Hf and Nd plot significantly above the depletion trend; their concentrations are governed by the equilibrium partitioning between percolating melt and peridotites. The distinct geochemical characteristics of type IIa and type IIb clinopyroxenes may have resulted from chromatographic percolation of small volumes of silicate melts, in which percolation fronts of incompatible elements are dependent on their relative incompatibilities.

1. Introduction

Constraints on composition and evolution of the lithospheric mantle may be provided by studies of basalt-borne peridotite xenoliths. A number of studies are now available on mantle xenoliths from eastern China (Song and Frey, 1989; Xu et al., 1998a, 2003, 2008; Gao et al., 2002; Rudnick et al., 2004; Xu and Bodinier, 2004; Wu et al., 2003, 2006; Zheng et al., 2001, 2006). Whereas trace element and Sr–Nd isotopic data are abundant for the Chinese subcontinental lithospheric mantle (SCLM), Lu/Hf isotopic data are still scare for these rocks, probably due to the analytical difficulty encountered in analyzing mantle minerals which commonly contain low Hf abundances (usually ⩽1 ppm in clinopyroxene and garnet). With the advent of multiple-collector inductively-coupled plasma mass spectrometry (MC-ICPMS), precise analyses of Hf isotopes in mantle samples has become routine (Blichert-Toft et al., 1997; Schmidberger et al., 2002; Bedini et al., 2004; Ionov et al., 2005, 2006; Wu et al., 2006). Compared to the Rb–Sr and Sm–Nd isotopic systems, the difference in compatibility between Lu and Hf in peridotite-melt systems is larger (e.g., Johnson, 1998; Salters and Longhi, 1999), implying that a significant fractionation of Lu/Hf ratio can occur during high degree partial melting and therefore generate a broad range of Hf isotopic variation within a given time span. Furthermore, Hf is more compatible than Sr and Nd in residual peridotites relative to melts or fluids. Therefore Lu and Hf are insensitive to some types of metasomatism and may better record earlier mantle depletion events. More importantly, the combination of the Nd–Hf isotopic systems is particularly useful in tracing the evolution of the lithosphere, because of the close to similar geochemical affinity of the two isotope systems, as attested to by oceanic basalts. Bizimis et al. (2003) were

* Corresponding author. Tel.: +86 20 85290109; fax: +86 20 85290130.
E-mail address: yigangxu@gig.ac.cn (Y.-G. Xu).

1367-9120/$ - see front matter © 2009 Elsevier Ltd. All rights reserved.
doi:10.1016/j.jseaes.2009.04.005

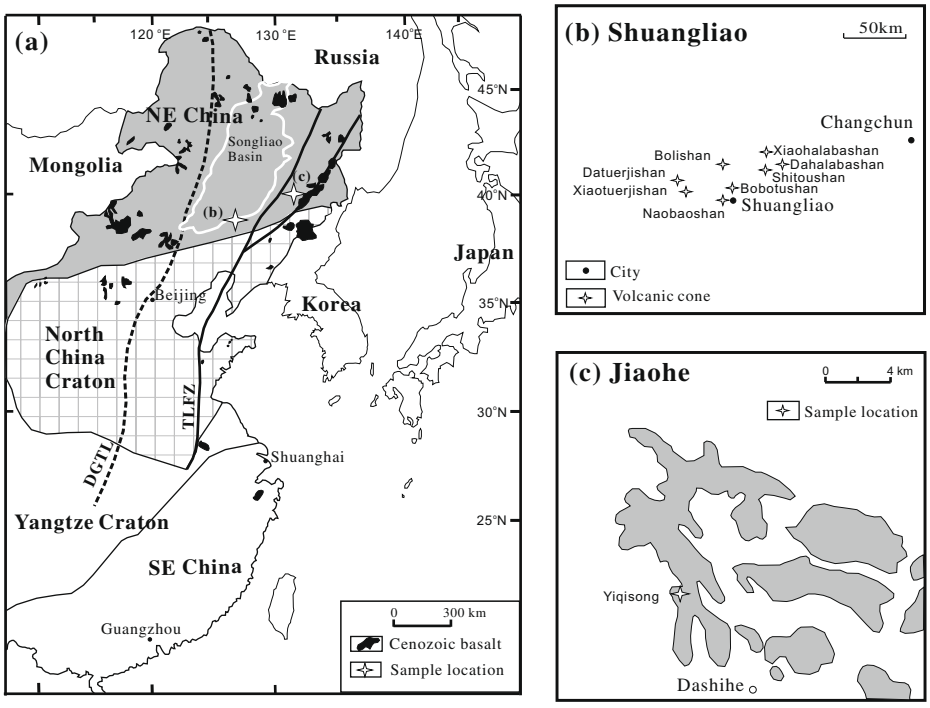

Fig. 1. (a) A sketch map showing the simplified tectonic framework of Eastern China and location of the studied area [modified after E and Zhao (1987)]. (b) and (c) are Enlarged sampling areas (marked in (a)) in Shuangliao and Jiaohe, Northeastern China. DGTL: Daxinganling-Taihangshan gravity lineament and TLFZ: Tancheng-Lujiang fault zone.

Table 1
Texture, modal composition, equilibrium temperatures (°C) of peridotite xenoliths from Shuangliao and Jiaohe.

	Texture	ol	opx	cpx	sp	$Cr\#_{sp}$	Fo	BM85	W77	WS
Type I										
BBT-8	Protogranular	58.7	29.7	10.2	1.3	0.13	0.898	1089	1068	1025
BLS-1	Porphyroclastic	59.4	24.4	12.8	2.8	0.1	0.893	886	914	903
BLS-3	Porphyroclastic	59	23	14.1	3.5	0.11	0.900	904	926	922
BLS-5	Protogranular	59.5	21.7	15.3	2.8	0.1	0.895	1017	1008	974
NBS-1	Equigranular	63.6	21.1	12.7	2.6	0.11	0.900	772	833	855
YQS-7	Equigranular	66.3	21.9	9	2.3	0.13	0.894	767	811	883
YQS-9	Porphyroclastic	61.8	20.8	14	2.8	0.1	0.898	840	873	907
Type IIa										
BBT-1	Protogranular	54.9	38	6.4	0.7	0.25	0.903	1052	1056	1065
BBT-2	Equigranular	80.2	14.8	3.6	1.2	0.4	0.911	876	909	885
BBT-4	Equigranular	70	26.1	3.6	0.7	0.37	0.909	803	856	891
BBT-5	Equigranular	70	23.7	6	0.8	0.29	0.905	797	849	845
BBT-7	Protogranular	84.3	11.7	3	1.3	0.36	0.911	1005	1024	1050
BLS-6	Protogranular	73.4	20	5	1.5	0.38	0.908	888	935	919
YQS-5	Equigranular	67.4	22.5	7.3	2.5	0.23	0.904	701	792	864
YQS-6	Equigranular	80.8	12.3	4.8	1.7	0.23	0.911	716	790	886
YQS-8	Protogranular	73.7	20.5	4	1.4	0.34	0.905	841	882	947
YQS-11	Protogranular	69.4	24.3	4.1	1.3	0.31	0.911	812	853	891
YQS-12	Protogranular	75.9	15.7	6	2	0.29	0.906	968	989	957
YQS-16	Protogranular	80.4	14.8	3.1	1.5	0.29	0.905	885	904	934
Type IIb										
BBT-6	Protogranular	85.5	10.9	2.3	1.1	0.39	0.910	1041	1036	1075
BBT-9	Protogranular	81.3	14.4	3.2	0.7	0.58	0.912	1055	1047	983
BBT-10	Protogranular	65.8	29.2	4.3	0.7	0.35	0.915	1058	1048	1078
BBT-11	Protogranular	56.9	37	5.7	0.5	0.31	0.904	1038	1045	1040
BLS-2	Porphyroclastic	82.9	13.1	2.6	1.2	0.5	0.912	932	934	930
YQS-1	Equigranular	65.7	22	9.6	2.3	0.16	0.903	713	799	866
YQS-2	Porphyroclastic	79.7	17.1	1.8	1	0.53	0.916	778	829	813
YQS-3	Porphyroclastic	80.8	14	3	2	0.19	0.901	748	825	866
YQS-4	Equigranular	73.8	20.7	3.8	1.4	0.28	0.910	728	795	868
YQS-10	Protogranular	75.5	16.8	6	1.7	0.36	0.907	813	863	876
YQS-14	Protogranular	75.6	18.9	3.5	1.8	0.37	0.911	812	875	915
YQS-15	Protogranular	80.5	10.2	6.7	2	0.39	0.907	858	877	893

ol, Olivine; opx, orthopyroxene; cpx, clinopyroxene; and sp, spinel. Modal compositions are calculated from bulk of least-squares regression method. Mg#, $Mg/(Mg + Fe)_{atom}$ and Cr#, $Cr/(Cr + Al)_{atom}$. Thermometers: BM85: two-pyroxene thermometer of Bertrand and Mercier (1985); W77: two-pyroxene thermometer of Wells (1977); WS: Cr–Al–opx thermometer of Witt-Eickschen and Seck (1991); pressure of 15 kbar are assumed in thermometric calculation.

the first to report significant Hf–Nd isotopic decoupling (i.e., Hf–Nd isotopes of samples significantly off the mantle array defined by oceanic basalts) in oceanic mantle lithosphere. Since then, Nd–Hf decoupling has frequently been observed in the continental mantle (Schmidberger et al., 2002; Salters and Zindler, 1995; Bizimis et al., 2003; Aulbach et al., 2004; Bedini et al., 2004; Carlson et al., 2004; Ionov et al., 2005, 2006; Wu et al., 2006; Simon et al., 2007; Choi et al., 2007; Bianchini et al., 2007). At least four models have been proposed for the origins of Hf–Nd isotope decoupling: (1) HREE redistribution related to spinel-garnet phase transition on isobaric cooling after the partial melting (Ionov et al., 2005). (2) Melting of mantle peridotite in the presence of garnet resulting in a significant fractionation of Lu/Hf and Sm/Nd ratios as garnet preferentially incorporates Lu relative to Hf, to a greater extent than Sm relative to Nd (Schmidberger et al., 2002). (3) Variable radiogenic Hf at a near constant Nd isotope composition attributable to melt–mantle interaction (Salters and Zindler, 1995; Bizimis et al., 2003). (4) Different Lu–Hf and Sm–Nd isotope behaviors stemming from variable metasomatism involving different metasomatic agents (Wittig et al., 2007).

In this paper, we present the first comprehensive study on major and trace element abundances, Hf, Nd and Sr isotopic compositions of clinopyroxene separates from spinel peridotite xenoliths from Shuangliao and Jiaohe, Northeastern China. The data allow us to identify three distinct geochemical types and significant decoupling of Hf from Nd isotopes in some samples. On the basis of evaluation of different trace elements during partial melting and mantle metasomatism, it is proposed that Nd–Hf isotopic decoupling likely resulted from selective pervasive mantle metasomatism. Implication on the genesis and evolution of the continental lithosphere beneath NE China is also discussed.

2. Geological setting and samples

Northeast China in the eastern part of the Paleozoic Central Asian Organic Belt (Fig. 1a) is a composite fold belt formed by amalgamation of several minor blocks during subduction and collision between the Siberian and North China Craton (Jahn et al., 2000). The final suturing of these two continents was not complete until Jurassic (Zhao et al., 1990). The Songliao basin in the central part of Northeast China is the largest basin in eastern China, covering 260,000 km^2. The basement of this basin consists of Paleozoic strata and Paleozoic to Mesozoic granites (Wu et al., 2001). Seismic and conductivity measurements suggest that the lithosphere at center of the basin is 80 km thick and thickens to about 120 km towards the margins.

The peridotite xenoliths studied in this paper were collected from Shuangliao and Jiaohe volcanic fields in Jilin Province. The Shuangliao volcanic field is located along southeastern edge of the Songliao basin, and consists of eight volcanoes: Bobotushan, Naobaoshan, Bolishan, Dahalabashan, Xiaohalabashan, Datuerjishan, Xiaotuerjishan, and Shitoushan (Fig. 1b). The eruptive rocks vary from dolerites to alkaline olivine basalt, with K–Ar ages ranging from 86 to 40 Ma (Yu, 1987; Liu, 1987). Five to fifteen centimetres diameter xenoliths included in these volcanics were selected for this study, 9 spinel lherzolites and 7 harzburgites, mainly from Bobotushan (BBT), Bolishan (BLS) and Naobaoshan (NBS) volcanoes.

The Jiaohe volcanic field in Jilin Province is located near the Northern part of the Tan-Lu fault zone. Cenozoic basalts (2–24 Ma, Wang, 1996) are widespread in Dashihe, Jiaohe city. Abundant fresh xenoliths, 5–25 cm in diameter, were discovered in a quarry of an olivine mine at Yiqisong (YQS, Fig. 1c). The xenoliths collected from this locality include spinel lherzolite, harzburgite and garnet pyroxenite. This last one will be the subject of a separated paper. The Shuangliao and Jiaohe xenoliths show similar mineralogical and petrological characters, which may be summarized as follows.

All studied xenoliths are anhydrous peridotites and belong to the Group I peridotites of Frey and Prinz (1978). Their typical mineral assemblage is olivine (ol, 56–86%), orthopyroxene (opx, 10–38%), clinopyroxene (cpx, 2–15%) and spinel (sp, 0.5–3.5%) (Table 1). Using the textural classification of Mercier and Nicolas (1975), we can distinguish three textural types that are, in order of increasing degree of deformation: (1) coarse-grained protogranular, (2) porphyroclastic and (3) equigranular.

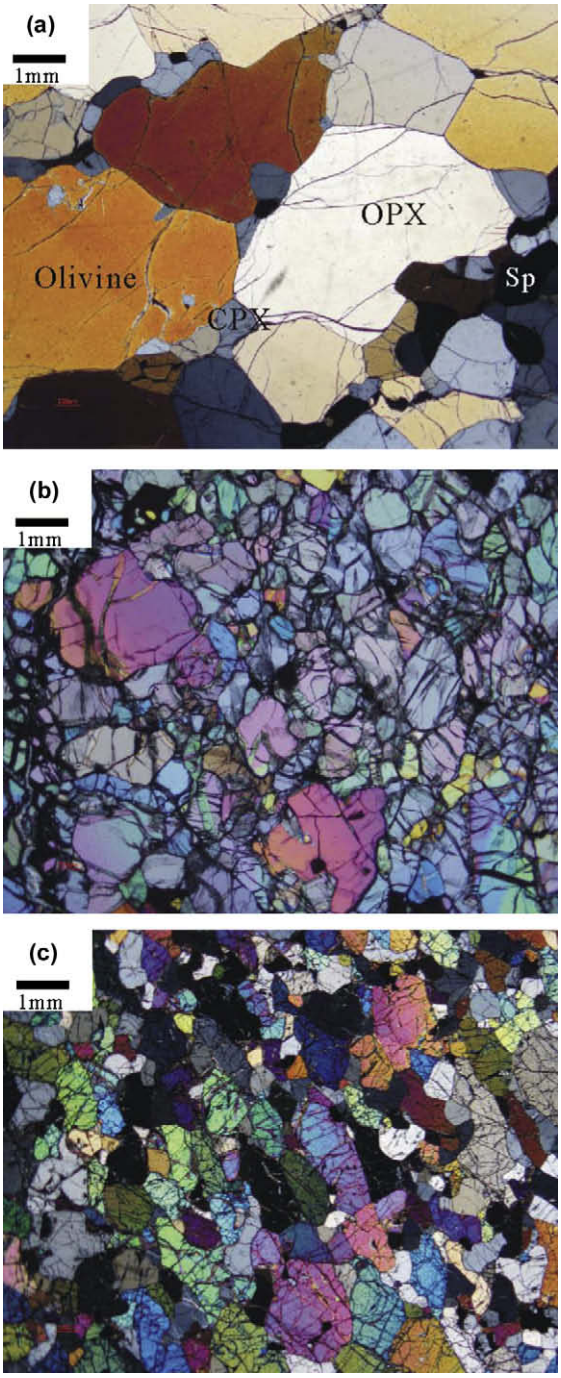

Fig. 2. Photomicrograph showing textures observed in Shuangliao and Jiaohe peridotite xenoliths (crossed polarizers). (a) Protogranular lherzolites; (b) porphyroclastic texture with orthopyroxene as porphyroclast; and (c) tabular equigranular texture with neoblasts defining a noticeable foliation.

Samples with protogranular texture (Fig. 2a) are the most abundant among the Shuangliao and Jiaohe xenolith populations. They are characterized by a coarse grain size of 4–5 mm. Olivine and orthopyroxene (opx) grains are equant and exhibit curvilinear grain boundaries. Exsolution lamellae are present in some large opx grains. Compared to the protogranular samples, the porphyroclastic peridotites contain more important amounts of small to median grained minerals (0.3–1 mm) with only a few porphyroclasts of orthopyroxene (Fig. 2b), reflecting a slightly greater degree of recrystallisation. Some samples have olivines with kink-bands and 120° angle triple junctions. Much smaller and homogeneous grains (<1 mm) are observed in the tabular equigranular samples (Fig. 2c). Most neoblasts show noticeable foliation (Fig. 2c). Grain boundaries with well developed 120° triple angles are frequent, and are interpreted to be the result of complete recrystallization. Some samples exhibit spongy textures of spinel with irregular shaped cpx and olivine at the rim.

Modal compositions (Table 1) were calculated by a least-square fit method using constituent mineral chemistry and bulk geochemistry. Consistent with the petrographic observations, xenoliths in this study range from relatively fertile lherzolite to clinopyroxene-poor lherzolite and harzburgites. Harzburgites occupy an important percentage (~70%) among the xenolith population (Fig. 3a), as compared to dominant lherzolite xenoliths from North China (Yu et al., 2007a). On a plot of olivine mode against Fo (i.e., $Mg\#_{ol}$) (Fig. 3b), most of the studied peridotites either fall in the area typical for Phanerozoic mantle or straddle the boundary between Phanerozoic and Proterozoic mantle.

3. Sample preparation and analytical methods

The xenoliths for this study were cut to remove exterior surfaces. Relatively fresh interiors without basaltic veins were used for bulk-rock analyses and for mineral separation. The rocks were crushed in a steel mortar and ground in a steel mill. Cpx from crushed rocks were handpicked under a binocular microscope and washed in an ultrasonic bath with Mill-Q ultra-pure water and leached with 6 N HCl for 30 min. Chemical analyses were performed at Guangzhou Institute of Geochemistry, Chinese Academy of Sciences (GIGCAS). Bulk major elements were measured by X-ray fluorescence. A subset of clinopyroxene separates were analyzed for trace elements including rare earth elements (REE) using an Inductively Coupled Plasma-Mass Spectrometer (ICP-MS), following analytical procedures described by Xu (2002). The analytical precision for most minor and trace elements is better than ±5%. For Sr–Nd isotopic analyses, cpx separates of 11 samples were dissolved in distilled HF–HNO_3 Savillex screwtop Teflon beakers at 150 °C for 10 days, Sr and REE were separated on columns made of Sr and REE resins of the Eichrom Company using 0.1% HNO_3 as elutant. Separation of Nd from the REE fractions was carried out on HDEHP columns with a 0.18 N HCl elutant. Samples were analyzed for Sr–Nd isotopic composition using a Micromass Isoprobe Multi-Collector ICPMS at GIGCAS. Analyses of standards during the period of analysis were as follows: international standard NBS987gave $^{87}Sr/^{86}Sr = 0.710262 \pm 17$ (2 SD), which falls within the uncertainty of the recommended value ($^{87}Sr/^{86}Sr = 0.710250 \pm 10$, McArthur, 1994); in-house standard Sr-GIG gave $^{87}Sr/^{86}Sr = 0.708844 \pm 23$ (2 SD). International standard JNdi-1 (recommended value: $^{143}Nd/^{144}Nd = 0.512115 \pm 7$, Tanaka et al., 2000) gave $^{143}Nd/^{144}Nd = 0.512123 \pm 10$ (2 SD); in-house standard Nd-GIG gave $^{143}Nd/^{144}Nd = 0.511525 \pm 10$ (2 SD).

For Hf isotopic analyses, powders of 0.5 g cpx separates mixed with 1 g $Li_2B_4O_7$ were fused to make glass discs at 1200 °C. About 0.3 g of the glass disc was digested by 2 N HCl, which was used for Hf separation on anion-exchange chromatography using BIORAD AG-1-8X resin with HCl + HF + H_2O_2 as elutant. Hf isotopic analyses were carried out on a double focusing Finnigan Neptune Multi-Collector ICP-MS at Institute of Geology and Geophysics, Chinese Academy of Sciences (IGGCAS), following the analytical procedure described by Li et al. (2005). Total procedual blanks for Hf were less than 30 pg. The results of Hf isotopic ratios was monitored by JMC475 Hf standard, for which the mean $^{176}Hf/^{177}Hf$ ratio is 0.282162 ± 10 (2σ) during the analytical period (the recommended $^{176}Hf/^{177}Hf$ value is 0.282160 ± 10 (2σ), Nowell et al., 1998).

4. Results

4.1. Mineral chemistry and equilibrium temperatures

Major element compositions of minerals in representative peridotites from this study are given in Table 2. No significant compositional difference was found between the xenoliths from Shuangliao and Jiaohe. The studied xenoliths display a wide range in mineral composition (Table 2), which matches the petrographic variation. $Mg\#_{ol}$ [$Mg/(Mg + Fe)_{at}$] in Shuangliao and Jiaohe peridotites ranges from 0.893 to 0.916 (Table 1). Spinels have a wide range of $Cr\#_{sp}$ ($Cr/(Cr + Al)_{at} = 0.10–0.58$, Table 1), showing a negative correlation with the mode of cpx (Fig. 4a). In the co-variation diagram of $Mg\#_{ol}$ versus $Cr\#_{sp}$ (Fig. 4b), the fertile lherzolites show a progressively increasing $Mg\#_{ol}$ at nearly constant $Cr\#_{sp}$, whereas refractory harzburgites samples exhibit a significant increase in $Cr\#_{sp}$ (from 0.16 to 0.58) and only a slight increase in $Mg\#_{ol}$. These compositional variations are similar to those defined by unmetasomatized peridotites from around the world, suggesting the primary control of partial melting on mineral composition (Jaques and Green, 1980; Cabanes and Mercier, 1988; Yaxley et al., 1998; Xu and Bodinier, 2004). Clinopyroxenes in fertile lherzolites have high Na_2O (1.2–1.9%), a common feature of mantle xenoliths.

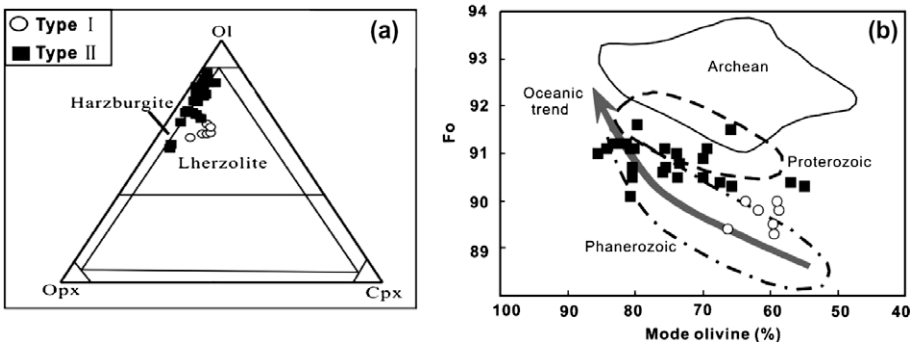

Fig. 3. (a) ol–cpx–opx Triangle plot for Shuangliao and Jiaohe peridotites. (b) Plot of olivine mode (%) vs. forsterite content ($Fo = 100 \times Mg/(Mg + Fe)_{atomic}$) for the Shuangliao and Jiaohe xenoliths. Oceanic trend and fields of Archean, Proterozoic and Phanerozoic mantle are from Griffin et al. (1999).

Table 2
Mineral composition (in wt%) of peridotite xenoliths from Shuangliao and Jiaohe.

	BBT-8				BLS-1				BLS-3				BLS-5			
	ol	opx	cpx	sp	ol	opx	cpx	sp	ol	opx	cpx	sp	ol	opx	cpx	sp
	Type 1															
Na_2O	0.02	0.18	1.37	0.01	0.01	0.10	1.43	0.02	0.03	0.11	1.56	0.01	0.02	0.15	1.54	0.02
SiO_2	41.02	53.91	51.12	0.10	41.06	55.15	51.89	0.05	40.90	54.77	51.49	10.18	40.95	53.99	51.44	0.07
MgO	48.91	32.56	15.87	20.56	49.15	33.95	15.21	20.96	49.35	33.97	15.35	27.88	49.18	33.45	15.54	20.62
MnO	0.14	0.15	0.09	0.13	0.14	0.15	0.08	0.13	0.14	0.14	0.08	0.13	0.14	0.15	0.08	0.12
TiO_2	0.05	0.18	0.55	0.28	0.02	0.12	0.42	0.12	0.03	0.13	0.52	0.13	0.03	0.14	0.47	0.20
Al_2O_3	0.03	5.10	6.81	54.29	0.01	3.94	5.89	57.77	0.01	3.94	6.22	42.20	0.03	4.82	6.48	57.83
CaO	0.10	1.15	18.68	0.01	0.05	0.63	20.75	0.00	0.05	0.69	20.42	0.05	0.07	0.94	19.26	0.00
NiO	0.12	0.13	0.07	0.39	0.13	0.12	0.08	0.46	0.13	0.12	0.04	0.43	0.14	0.13	0.08	0.43
FeO	9.96	6.24	3.53	12.16	10.64	6.52	2.74	10.90	9.85	6.40	2.81	10.91	10.40	6.47	3.34	10.74
Cr_2O_3	0.04	0.46	0.75	11.97	0.01	0.27	0.61	9.64	0.05	0.33	0.75	7.90	0.00	0.36	0.62	9.36
Total	100.34	99.96	98.85	99.90	101.20	100.95	99.08	100.03	100.51	100.59	99.25	99.77	100.93	100.59	98.82	99.37
Mg#	0.898	0.904	0.890	0.753	0.893	0.904	0.909	0.776	0.900	0.905	0.908	0.821	0.895	0.903	0.893	0.776
	NBS-1				YQS-7				YQS-9				BBT-1			
	Type 1												Type IIa			
Na_2O	0.01	0.04	1.26	0.02	0.01	0.05	1.83	0.03	0.04	0.08	1.81	0.02	0.01	0.07	0.80	0.03
SiO_2	40.85	55.45	51.34	0.03	41.27	55.59	52.08	0.03	41.30	55.33	51.96	0.02	41.18	54.95	52.22	0.11
MgO	49.48	34.72	15.28	20.88	49.06	34.60	14.42	19.98	48.79	34.07	14.60	20.63	49.72	33.72	16.86	19.27
MnO	0.16	0.14	0.09	0.13	0.14	0.16	0.07	0.12	0.15	0.15	0.07	0.11	0.13	0.15	0.09	0.18
TiO_2	0.02	0.14	0.62	0.10	0.02	0.12	0.50	0.06	0.02	0.12	0.55	0.12	0.03	0.08	0.12	0.13
$A1_2O_3$	0.02	3.28	5.57	57.62	0.00	3.34	6.20	55.64	0.01	3.82	6.49	58.03	0.04	4.07	4.83	44.86
CaO	0.03	0.41	21.78	0.00	0.02	0.43	21.01	0.02	0.01	0.48	20.56	0.00	0.09	1.11	20.28	0.00
NiO	0.14	0.13	0.06	0.44	0.13	0.12	0.07	0.37	0.13	0.13	0.04	0.44	0.13	0.14	0.05	0.38
FeO	9.85	6.37	2.63	10.27	10.43	6.64	2.27	11.16	9.95	6.48	2.62	10.56	9.64	6.26	3.09	13.19
Cr_2O_3	0.05	0.23	0.68	10.32	0.03	0.30	0.93	12.30	0.02	0.30	0.80	9.86	0.02	0.58	0.92	22.05
Total	100.58	100.91	99.31	99.81	101.09	101.34	99.38	99.69	100.38	100.96	99.51	99.80	100.99	101.13	99.25	100.18
Mg#	0.900	0.907	0.913	0.785	0.894	0.904	0.919	0.763	0.898	0.904	0.909	0.779	0.903	0.907	0.908	0.724
	BBT-2				BBT-4				BBT-5				BBT-7			
	Type IIa															
Na_2O	0.01	0.04	1.21	0.03	0.02	0.06	1.20	0.04	0.01	0.03	1.17	0.02	0.02	0.09	0.70	0.04
SiO_2	40.93	55.95	52.76	0.02	41.25	56.23	53.17	0.05	41.07	56.43	52.92	0.04	41.02	55.03	52.23	0.13
MgO	49.49	35.14	16.03	17.71	49.76	35.21	15.93	17.33	49.78	35.67	15.82	17.68	49.08	33.92	16.90	18.36
MnO	0.12	0.14	0.06	0.18	0.13	0.14	0.07	0.23	0.12	0.14	0.09	0.22	0.14	0.12	0.08	0.19
TiO_2	0.02	0.04	0.08	0.09	0.03	0.02	0.09	0.05	0.03	0.04	0.07	0.09	0.01	0.06	0.13	0.16
Al_2O_3	0.01	2.13	3.35	37.90	0.01	2.17	3.31	35.90	0.02	1.91	3.25	35.05	0.02	3.46	4.07	41.70
CaO	0.03	0.42	21.16	0.01	0.03	0.50	21.84	0.01	0.02	0.40	21.79	0.01	0.09	1.00	20.91	0.02
NiO	0.18	0.12	0.03	0.22	0.14	0.09	0.05	0.22	0.14	0.07	0.03	0.18	0.12	0.13	0.05	0.35
FeO	8.67	5.41	2.11	11.32	8.87	5.59	2.14	12.21	8.71	5.64	2.09	11.70	9.22	5.75	2.78	13.11
Cr_2O_3	0.01	0.43	1.27	31.12	0.02	0.44	1.31	33.88	0.04	0.35	1.23	35.35	0.03	0.60	0.92	25.93
Total	99.47	99.82	98.06	98.60	100.23	100.45	99.13	99.91	99.90	100.68	98.43	100.32	99.74	100.18	98.76	99.96
Mg#	0.911	0.921	0.932	0.738	0.910	0.919	0.930	0.719	0.911	0.919	0.931	0.731	0.905	0.914	0.916	0.716
	BLS-6				YQS-5				YQS-6				YQS-8			
	Type IIa															
Na_2O	0.00	0.05	0.76	0.01	0.02	0.02	0.65	0.02	0.02	0.05	1.19	0.00	0.03	0.05	1.20	0.01
SiO_2	40.87	55.94	52.98	0.03	41.15	55.99	52.38	0.03	41.20	56.01	52.66	0.02	41.33	56.03	53.19	0.03
MgO	49.54	34.93	16.91	17.30	49.45	35.03	16.03	18.02	49.92	35.18	15.66	19.28	49.77	35.05	16.02	17.51
MnO	0.12	0.13	0.06	0.23	0.12	0.14	0.06	0.17	0.13	0.17	0.07	0.19	0.15	0.14	0.08	0.22
TiO_2	0.01	0.03	0.08	0.11	0.01	0.05	0.16	0.06	0.01	0.04	0.11	0.05	0.03	0.01	0.09	0.09
Al_2O_3	0.02	2.42	3.00	36.13	0.01	2.41	3.53	46.07	0.00	2.88	4.14	47.71	0.01	2.60	3.62	39.31
CaO	0.06	0.71	22.02	0.00	0.03	0.39	23.27	0.01	0.01	0.42	22.38	0.01	0.03	0.59	21.68	0.00
NiO	0.14	0.13	0.04	0.23	0.13	0.06	0.03	0.31	0.14	0.06	0.04	0.29	0.13	0.07	0.08	0.27
FeO	9.01	5.47	2.29	13.27	9.45	6.20	2.21	14.50	8.79	5.71	2.02	11.81	9.37	6.00	2.29	13.81
Cr_2O_3	0.02	0.49	0.97	32.55	0.00	0.35	0.82	21.09	0.05	0.35	1.08	21.15	0.01	0.48	1.24	29.68
Total	99.75	100.29	99.12	99.84	100.37	100.62	99.12	100.29	100.25	100.86	99.34	100.49	100.84	100.99	99.49	100.92
Mg#	0.908	0.920	0.930	0.701	0.904	0.910	0.929	0.691	0.911	0.917	0.933	0.746	0.905	0.913	0.926	0.695
	YQS-11				YQS-12				YQS-16				BBT-6			
	Type IIa												Type IIb			
Na_2O	0.03	0.07	1.30	0.02	0.02	0.09	0.87	0.03	0.01	0.07	1.45	0.01	0.01	0.10	1.14	0.03
SiO_2	41.45	56.53	53.16	0.02	41.30	55.68	52.83	0.05	41.31	55.99	52.98	0.04	40.85	55.20	52.22	0.09
MgO	50.42	35.26	15.84	18.36	49.64	34.29	16.63	18.76	49.96	35.00	15.73	18.62	49.45	33.96	16.75	17.70
MnO	0.13	0.14	0.07	0.17	0.12	0.12	0.10	0.17	0.13	0.15	0.08	0.19	0.11	0.14	0.08	0.23
TiO_2	0.02	0.05	0.14	0.08	0.00	0.07	0.15	0.12	0.01	0.05	0.19	0.11	0.03	0.05	0.10	0.15
Al_2O_3	0.02	2.45	3.88	41.45	0.01	3.17	3.92	42.86	0.02	2.88	4.34	43.17	0.02	3.21	4.16	35.61

Table 2 (*continued*)

	YQS-11				YQS-12				YQS-16				BBT-6			
	Type IIa												Type IIb			
CaO	0.03	0.53	21.74	0.00	0.05	0.84	21.18	0.00	0.05	0.56	21.00	0.00	0.11	1.05	19.77	0.01
NiO	0.39	0.35	0.12	0.83	0.13	0.14	0.03	0.31	0.14	0.12	0.08	0.33	0.14	0.11	0.10	0.24
FeO	8.89	5.46	2.00	11.83	9.22	5.69	2.57	12.40	9.40	5.84	2.08	11.97	8.90	5.53	2.83	13.32
Cr_2O_3	0.05	0.41	1.08	28.32	0.04	0.51	1.06	25.75	0.02	0.48	1.33	25.91	0.02	0.73	1.16	31.51
Total	101.36	101.26	99.33	101.08	100.52	100.59	99.35	100.45	101.05	101.15	99.25	100.35	99.61	100.07	98.29	98.88
Mg#	0.911	0.921	0.934	0.736	0.906	0.916	0.921	0.731	0.905	0.915	0.932	0.737	0.909	0.917	0.914	0.705
	BBT-9				BBT-10				BBT-11				BLS-2			
	Type IIb															
Na_2O	0.02	0.08	1.02	0.02	0.01	0.10	1.08	0.01	0.01	0.08	0.77	0.02	0.01	0.13	1.76	0.02
SiO_2	41.36	55.97	52.92	0.07	41.02	55.19	52.34	0.09	41.29	54.27	51.87	0.09	41.04	56.13	53.27	0.04
MgO	49.94	34.74	17.23	15.73	50.16	34.28	16.88	18.62	49.62	33.70	16.98	18.54	49.98	35.37	16.03	16.46
MnO	0.11	0.14	0.08	0.27	0.15	0.13	0.09	0.20	0.12	0.15	0.08	0.20	0.10	0.14	0.08	0.27
TiO_2	0.02	0.07	0.15	0.42	0.03	0.09	0.20	0.29	0.04	0.09	0.15	0.24	0.02	0.03	0.10	0.15
Al_2O_3	0.02	2.06	3.00	22.14	0.01	3.40	4.42	37.71	0.03	3.68	4.23	39.69	0.03	1.93	3.58	27.53
CaO	0.10	1.07	19.92	0.00	0.09	1.07	19.88	0.01	0.11	1.14	20.34	0.02	0.04	0.67	20.01	0.00
NiO	0.14	0.13	0.06	0.19	0.13	0.10	0.07	0.26	0.15	0.08	0.09	0.36	0.14	0.10	0.05	0.19
FeO	8.64	5.31	2.68	16.55	8.35	5.25	2.74	12.13	9.52	5.85	2.97	14.19	8.71	5.34	2.27	14.05
Cr_2O_3	0.05	0.70	1.34	45.13	0.04	0.81	1.33	30.40	0.03	0.66	0.96	26.31	0.04	0.56	1.59	41.65
Total	100.40	100.27	98.39	100.51	99.97	100.41	99.01	99.72	100.87	99.71	98.45	99.63	100.08	100.39	98.74	100.36
Mg#	0.912	0.922	0.921	0.631	0.915	0.922	0.917	0.734	0.904	0.912	0.911	0.702	0.912	0.923	0.927	0.678
	YQS-1				YQS-2				YQS-3				YQS-4			
	Type IIb															
Na_2O	0.00	0.02	0.58	0.01	0.02	0.03	1.22	0.00	0.01	0.03	0.70	0.00	0.01	0.02	1.14	0.01
SiO_2	41.16	55.57	52.13	0.07	41.28	57.14	54.03	0.03	41.09	55.58	52.36	0.02	41.01	56.17	52.89	0.02
MgO	49.61	34.96	16.04	19.33	50.36	36.00	16.18	14.53	49.53	34.87	16.12	18.96	49.86	35.24	15.80	18.05
MnO	0.13	0.15	0.07	0.15	0.12	0.13	0.08	0.31	0.12	0.15	0.08	0.16	0.12	0.13	0.08	0.19
TiO_2	0.00	0.06	0.14	0.03	0.01	0.04	0.05	0.06	0.04	0.06	0.10	0.04	0.02	0.06	0.17	0.05
Al_2O_3	0.01	2.92	3.80	52.09	0.00	1.37	2.37	25.65	0.00	2.78	3.60	50.18	0.01	2.33	3.60	43.56
CaO	0.01	0.42	23.30	0.01	0.01	0.46	22.10	0.00	0.02	0.41	22.89	0.01	0.02	0.46	22.41	0.00
NiO	0.15	0.12	0.08	0.42	0.14	0.09	0.08	0.17	0.15	0.11	0.04	0.34	0.15	0.08	0.04	0.29
FeO	9.57	6.39	2.34	12.57	8.34	5.43	1.88	16.36	9.82	6.27	2.15	12.58	8.90	5.81	1.89	12.66
Cr_2O_3	0.02	0.30	0.73	15.23	0.00	0.33	1.40	43.59	0.02	0.31	0.74	18.09	0.05	0.37	1.17	25.37
Total	100.64	100.90	99.19	99.86	100.27	101.01	99.40	100.70	100.75	100.57	98.75	100.37	100.09	100.66	99.19	100.20
Mg#	0.903	0.908	0.925	0.735	0.916	0.923	0.939	0.615	0.901	0.909	0.931	0.731	0.910	0.916	0.938	0.720
	YQS-10				YQS-14				YQS-15							
	Type IIb															
Na_2O	0.02	0.03	0.78	0.02	0.00	0.03	0.77	0.01	0.01	0.06	2.21	0.03				
SiO_2	41.38	56.45	53.23	0.01	41.15	56.16	53.13	0.03	41.32	56.27	54.31	0.03				
MgO	49.87	35.01	16.44	17.09	49.88	34.06	16.47	17.51	49.65	35.04	15.38	16.80				
MnO	0.13	0.15	0.08	0.21	0.12	0.12	0.06	0.24	0.14	0.12	0.06	0.23				
TiO_2	0.02	0.07	0.15	0.15	0.01	0.04	0.05	0.09	0.00	0.09	0.23	0.17				
Al_2O_3	0.01	2.30	2.98	37.81	0.00	2.41	2.91	36.74	0.00	2.26	3.59	34.80				
CaO	0.03	0.51	22.58	0.03	0.06	0.53	22.57	0.00	0.03	0.56	19.93	0.01				
NiO	0.38	0.27	0.15	0.64	0.22	0.11	0.04	0.25	0.13	0.13	0.07	0.23				
FeO	9.16	5.72	2.06	13.53	8.78	5.60	1.93	12.92	9.11	5.58	2.38	14.20				
Cr_2O_3	0.02	0.40	0.94	31.18	0.02	0.48	1.14	32.79	0.02	0.44	1.27	33.57				
Total	101.01	100.91	99.40	100.64	100.22	99.53	99.07	100.56	100.41	100.55	99.42	100.05				
Mg#	0.907	0.917	0.935	0.695	0.911	0.916	0.939	0.709	0.907	0.919	0.921	0.680				

Mg# = $Mg/(Mg + Fe)_{atomic}$.

Clinopyroxenes in refractory peridotites also show fairly high Na contents (0.6–2.2%), which are significantly higher than expected from the partial melting trends (Fig 4c). It appears that most refractory peridotites have been affected by metasomatism after partial melting.

Temperatures were estimated using the two-pyroxene thermometers of Bertrand and Mercier (1985) and Wells (1977) and the empirical thermometer (Witt-Eickschen and Seck, 1991), based on Cr–Al exchange between opx and spinel. For a given sample, these three thermometers yield similar estimates (Table 1), consistent with the homogeneous mineral composition. There is no significant difference between temperatures for the fertile and refractory samples (Table 1). The Shuangliao peridotites show a wide range of equilibrium temperature (833–1068 °C, using the thermometer of Wells (1977)), whereas the Jiaohe peridotites tend to have a lower and narrower temperature range (790–989 °C).

4.2. Whole rock chemistry

Whole rock compositions are collected in Table 3 and plotted in Fig. 5. The Shuangliao and Jiaohe peridotites show a considerable spread in major element composition, ranging from fertile lherzolites to refractory harzburgites with up to 46% MgO. Bulk rock geochemistry is controlled by modal phase compositions as indicated by the correlation between modal contents of clinopyroxene and $Cr\#_{sp}$ (Fig. 4a). Most samples lie along the partial melting trends in Fig. 5, and are interpreted as residues of variable degrees of partial melting (Frey et al., 1985; Takazawa et al., 2000).

4.3. Trace elements in clinopyroxene separates

For descriptional convenience, the peridotites from Shuangliao and Jiaohe are divided into two types (type I and type II) based on degree of partial melting and trace element composition (Fig. 6). Type I peridotites are generally fertile lherzolites, formed by relatively low degree of partial melting (0–5%), and characterized by LREE depletion. In contrast, type II peridotites are refractory, formed by a relatively high degree of partial melting (8–18%). Type II peridotites, characterized by LREE enrichment, can be further divided into type IIa and type IIb according to their variable degree of Hf enrichment (Fig. 6).

Clinopyroxene in Type I peridotites shows a LREE-depleted pattern ($(Ce/Yb)_n$ = 0.22–0.63) and high HREE contents ($(Ho/Yb)_n$ = 1.03–1.15, Table 4, Fig. 7a). They possess weak negative anomalies of Zr and Ti relative to the neighbouring REEs (Fig. 7b). Two samples (BLS-5, NBS-1) show inflection of La and Ce, coupled with relatively high contents of Th and U in cpx (Fig. 7a and b). Similar REE distribution patterns have been observed in both oceanic and continental xenoliths (Stosch and Seck, 1980; Menzies et al., 1985; Johnson et al., 1990; Downes and Dupuy, 1987; Song and Frey, 1989).

Clinopyroxene in Type II peridotites show LREE enriched patterns (Fig. 7c–f). Specifically, cpx from type IIa peridotites are either selectively enriched in LREE with a flat MREE-HREE pattern (e.g., YQS-8; BBT-1), or enriched in LREE and MREE with a flat HREE pattern (e.g., YQS-11; BBT-2). The enrichment of LREE is moderate with $(Ce/Yb)_n$ varying between 0.77 and 4.06, and is characterized by a slight convex-upward LREE segment (Fig. 7c). LREE enrichment is coupled with positive Th, U and Sr anomalies and negative high field strength element (HFSE) anomalies (with exception of BBT-4). Hf abundances in cpx are relatively low ranging from 0.12 to 0.43 ppm and plot along or slightly above the partial melting trend (Fig. 6c), suggesting that Hf contents in cpx from type IIa peridotites are either unaffected or only slightly affected by metasomatic processes. In contrast, Nd content in cpx plots significantly above the depletion trend, reflecting significant alteration of this element by metasomatism.

Type IIb clinopyroxenes differ from type IIa ones in stronger LREE enrichment ($(Ce/Yb)_n$ = 1.7–18.3). Specifically, La content can be as high as 90 times that of chondrite (Fig. 7e). Similar to type IIa samples, some type IIb peridotites exhibit negative HFSE anomalies (e.g., YQS-1; YQS-3). However, other samples (e.g., BBT-11; BLS-2) show weak or no HFSE anomalies. Despite this complexity, Hf abundances in cpx from type IIb peridotites tend to be higher (0.21–1.92 ppm) than those in type IIa peridotites. Both Hf and Nd plot significantly off the depletion trend (Fig 6c and d), suggesting a significant modification of these two elements by metasomatism.

Another noteworthy point is that LREE fractionation appears to be correlated with degree of depletion (Fig. 5e). The negative correlation between $(Ce/Yb)_n$ and MgO indicates that LREE enrichment is preferentially associated with those samples which were previously strongly depleted in basaltic and other incompatible components. Based on these observations, we can establish a relation between increasing LREE enrichment and increasing degree of melt extraction.

4.4. Sr–Nd–Hf isotope systematics in clinopyroxene separates

Clinopyroxene from Shuangliao and Jiaohe xenoliths exhibit a wide isotopic range (ε_{Nd} = −1.27 to 15.97, $^{87}Sr/^{86}Sr$ = 0.702649–0.707004 and ε_{Hf} = 7.9–63.8, Table 5). This is typical of suites of spinel peridotite xenoliths from single localities (Menzies et al., 1985; Stosch and Lugmair, 1986; Stosch et al., 1986; McDonough and McCulloch, 1987; Roden et al., 1988; Ionov et al., 1992), reflecting the large isotopic heterogeneity in continental lithospheric mantle. The observed isotopic variation is significantly larger than that exhibited by the host basalts (Fig. 8a), ruling out any genetic link between peridotite xenoliths and the host basalts. Moreover, different types of xenoliths, classified in terms of trace element compositions, show distinct isotopic compositions.

Clinopyroxenes from type I peridotites show high ε_{Nd} (>10) and low $^{87}Sr/^{86}Sr$ (<0.7031), falling within or plot above the MORB field. In contrast, type II peridotites display much higher $^{87}Sr/^{86}Sr$ (>0.7029) and lower ε_{Nd} (<9). Although type IIa and IIb clinopyroxenes generally overlap in the Sr–Nd isotopic space, available data suggest that type IIb cpx tend to have higher $^{87}Sr/^{86}Sr$ (i.e., EMII – enriched mantle II trend: $^{143}Nd/^{144}Nd$ = 0.5131–0.5133, $^{87}Sr/^{86}Sr$ = 0.707), whereas type IIa cpx evolve to lower ε_{Nd} at relatively low $^{87}Sr/^{86}Sr$ (i.e., EMI – enriched mantle I trend: $^{143}Nd/^{144}Nd$ = 0.5123–0.5124, $^{87}Sr/^{86}Sr$ = 0.7045–0.7060, Zindler and Hart, 1986).

Compared to the Nd isotopic composition, a wider range in Hf isotopes (ε_{Hf} = 7.9–63.8) is observed for the studied xenoliths, consistent with more significant Lu–Hf fractionation than Sm–Nd fractionation during partial melting. Three geochemical types of studied peridotites can be easily distinguished on a plot of ε_{Nd} versus ε_{Hf} (Fig. 8b). Clinopyroxene from Type I peridotites are

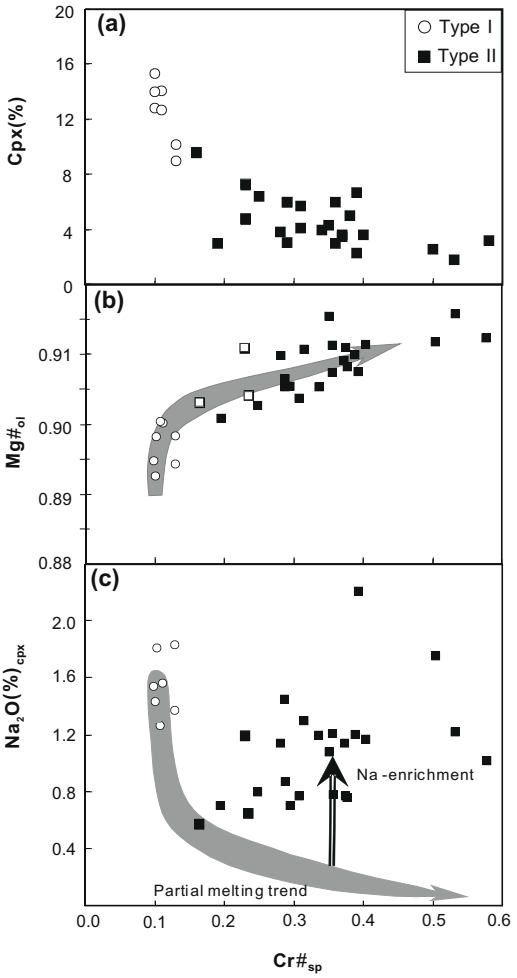

Fig. 4. Diagram illustrating modal composition and concentration of selected elements in different minerals from Shuangliao and Jiaohe peridotites. (a) Plot of mode of clinopyroxene versus Cr# [Cr# = $Cr/(Cr + Al)_{atomic}$] in spinel. (b) Correlation of Mg# in olivine versus Cr# of spinel. The partial melting trend is from Xu et al. (1998b). (c) Na_2O content in clinopyroxene versus Cr# of spinel.

plotted at the extension of the mantle array defined by oceanic basalts (Fig. 8b). Despite the moderate variation in Nd isotopic composition, type IIa clinopyroxenes display extremely radiogenic Hf isotope compositions (ε_{Hf} = 44.4–63.8), markedly off the mantle array. Similar decoupled Nd–Hf isotope character has been observed in previous studies (Ionov et al., 2005; Salters and Zindler, 1995; Bizimis et al., 2003; Wittig et al., 2007; Schmidberger et al., 2002). Type IIb clinopyroxenes have much lower Hf isotopic ratios, with ε_{Hf} ranging from ratios similar to the depleted mantle (Zindler and Hart, 1986) to values slightly more enriched than present day Bulk Earth values (Fig 8b). Isotope compositions of this group plot within and/or proximal to the OIB field.

Similar to what observed in Wangqing xenoliths (Xu et al., 1998a), Sr–Nd isotope ratios are correlated with the degree of LREE enrichment (using $(Ce/Yb)_n$ as a measure) (Fig. 9). Hf isotopes of cpx from type I and type IIa peridotites define a good negative correlation with $(Ce/Yb)_n$, whereas Hf isotopes of type IIb clinopyroxenes show no correlation between Hf isotope ratios and $(Ce/Yb)_n$. In the Sm–Nd isochron diagram (Fig. 10a), although $^{143}Nd/^{144}Nd$ positively correlates with $^{147}Sm/^{144}Nd$ for the Shuangliao and Jiaohe peridotites, the trend more likely reflects the complex mixing processes without significance as to age. Three LREE-depleted samples (BLS-1, BLS-5, YQS-9) define a line passing through the Bulk Earth point. Linear regression of the data yields an age of 1.2 Ga. A Proterozoic mantle is also suggested by Nd model ages of type I peridotites (1.3–1.7 Ga, Table 5). In the Lu–Hf isochron diagram (Fig 10b), no correlation is found between $^{176}Hf/^{177}Hf$ and $^{176}Lu/^{177}Hf$.

5. Discussion

5.1. Evidence for a Proterozoic mantle beneath NE China

The Shuangliao and Jiaohe peridotites delineate a sequence from primitive lherzolite through cpx-poor lherzolite to highly depleted harzburgite. In Fig. 4b, all the studied peridotites define a correlation between $Cr\#_{sp}$ and $Mg\#_{ol}$, which is in accordance with experimental data (Jaques and Green, 1980) and studies on natural samples (Cabanes and Mercier, 1988). Specifically, type I peridotites show low and restricted $Cr\#_{sp}$, indicating a low degree of partial melting. Refractory type II peridotites show a large variation of $Cr\#_{sp}$ (0.16–0.58) corresponding to moderate to high degrees of partial melting. These observations are consistent with whole rock major element composition (Fig. 5). For instance, in the diagrams of CaO and Al_2O_3 versus MgO, most of the Shuangliao and Jiaohe peridotites are within the field of peridotites worldwide and compositionally follow the modeled partial melting trend of Niu (1997), which are interpreted as residues of variable degree of partial melting (Frey et al., 1985; Takazawa et al., 2000, and references therein). Modeling the behavior of immobile elements during fractional melting within the spinel stability field (Johnson et al., 1990; Norman, 1998) suggests that type I peridotites are residues generated by relatively lower degrees of partial melting (5%), whereas type II peridotites were formed through higher degrees of partial melting (8–18%, Fig. 6a).

Clinopyroxene in Type I peridotites have $(Sm/Nd)_n > 1$ and plot within the field above that of MORB on the Sr–Nd isotope diagram (Fig. 8). This is consistent with derivation from a mantle depleted

Table 3
Major element compositions (in wt%) of whole rock peridotites from Shuangliao and Jiaohe.

	SiO_2	TiO_2	Al_2O_3	CaO	Cr_2O_3	NiO	MnO	Fe_2O_3	MgO	K_2O	Na_2O	P_2O_5	Total
Type I													
BBT-8	44.38	0.12	2.90	2.30	0.43	0.25	0.12	8.78	39.43	0.01	0.21	0.01	98.94
BLS-1	43.77	0.09	3.21	2.82	0.37	0.19	0.14	10.43	38.93	0.01	0.22	0.00	100.16
BLS-3	44.17	0.12	3.17	3.12	0.39	0.18	0.14	9.83	39.57	0.01	0.26	0.00	100.95
BLS-5	43.54	0.13	3.52	3.17	0.37	0.18	0.14	10.64	38.56	0.03	0.28	0.01	100.56
NBS-1	43.32	0.07	2.83	2.86	0.38	0.21	0.13	9.16	40.33	0.03	0.17	0.00	99.50
YQS-7	43.59	0.08	2.43	2.03	0.34	0.20	0.14	10.71	40.86	0.01	0.00	0.01	99.95
YQS-9	43.60	0.12	3.24	2.99	0.41	0.20	0.14	9.36	39.04	0.00	0.04	0.01	99.04
Type IIa													
BBT-1	45.55	0.04	2.13	1.74	0.47	0.25	0.12	8.52	40.18	0.01	0.09	0.02	99.12
BBT-2	41.88	0.01	0.89	0.71	0.40	0.20	0.12	9.17	45.65	0.02	0.07	0.00	99.13
BBT-4	41.98	0.00	0.79	0.59	0.36	0.19	0.13	9.18	46.22	0.00	0.05	0.00	99.50
BBT-5	41.89	0.01	0.81	0.84	0.36	0.19	0.13	9.34	44.46	0.03	0.05	0.01	98.10
BBT-7	43.76	0.03	1.38	1.55	0.37	0.19	0.12	8.80	42.35	0.01	0.08	0.00	98.65
BLS-6	43.30	0.01	1.17	1.27	0.45	0.21	0.13	9.38	43.76	0.00	0.05	0.00	99.72
YQS-5	43.55	0.02	1.74	1.81	0.41	0.21	0.14	9.81	42.04	0.00	0.00	0.01	99.46
YQS-6	41.98	0.01	1.31	1.13	0.34	0.19	0.13	9.46	44.86	0.01	0.00	0.07	99.90
YQS-8	43.31	0.01	1.15	1.01	0.34	0.21	0.14	10.08	43.74	0.01	0.00	0.01	99.59
YQS-11	43.82	0.02	1.32	1.02	0.41	0.20	0.12	8.48	43.59	0.02	0.00	0.01	99.18
YQS-12	42.88	0.02	1.59	1.42	0.46	0.19	0.13	9.56	43.94	0.00	0.00	0.00	100.04
YQS-16	42.52	0.02	1.20	0.78	0.35	0.19	0.13	9.96	45.30	0.01	0.00	0.01	100.02
Type IIb													
BBT-6	44.39	0.06	1.29	1.06	0.41	0.20	0.12	8.57	43.73	0.06	0.08	0.01	99.99
BBT-9	42.42	0.04	0.77	0.87	0.40	0.20	0.12	8.60	45.27	0.01	0.06	0.01	98.76
BBT-10	44.32	0.05	1.43	1.21	0.52	0.29	0.11	7.69	42.89	0.03	0.09	0.01	98.65
BBT-11	45.39	0.04	1.76	1.63	0.49	0.27	0.12	8.34	40.66	0.01	0.08	0.02	98.80
BLS-2	42.60	0.01	0.81	0.65	0.49	0.18	0.12	9.18	46.44	0.00	0.07	0.01	100.57
YQS-1	43.46	0.02	2.07	2.33	0.41	0.20	0.14	9.73	41.26	0.01	0.00	0.00	99.47
YQS-2	42.71	0.01	0.61	0.48	0.40	0.19	0.12	8.70	45.75	0.01	0.00	0.02	99.31
YQS-3	42.07	0.02	1.38	0.76	0.46	0.20	0.13	10.45	45.10	0.01	0.00	0.01	100.44
YQS-4	43.46	0.01	1.14	0.97	0.38	0.20	0.13	9.48	44.37	0.01	0.00	0.00	99.83
YQS-10	43.47	0.02	1.18	1.45	0.45	0.21	0.13	9.66	44.18	0.01	0.00	0.02	100.94
YQS-14	42.97	0.02	1.32	0.93	0.52	0.21	0.13	9.02	44.37	0.02	0.00	0.05	100.02
YQS-15	42.50	0.03	1.10	1.37	0.59	0.22	0.13	10.13	44.56	0.01	0.00	0.05	100.37

Note: 0.00 means that its content is below the detection limit.

in LREE and Rb for a sufficiently long time period. As type I peridotites (i.e., BLS-1, BLS-3, BLS-5, YQS-9) represent those mantle fragments which did not suffer any significant metasomatic alteration, they may have largely preserved the Nd and Sr isotope signatures of partial melting events and retain important information about mantle protolith and age of depletion. The calculated Nd model age for these peridotites using a single stage model from a primitive mantle is between 1307 and 1725 Ma (Table 5). There is an apparent isochron of 1.2 Ga passing through the bulk Earth defined by three LREE-depleted samples from type I peridotites (Fig. 10a).

Fig. 11a shows the modeled variation in ε_{Nd} and ε_{Hf} for mantle residues of different ages, illustrating the effect of melting degree and ages of the lithospheric mantle on Nd–Hf isotopic systematics. It appears that type I peridotites tend to follow modeled curves for ancient melting residues (>500 Ma), rather for a young mantle (100 Ma). In addition, the observed ε_{Nd} and ε_{Hf} for type I peridotites correspond to those for ~12% melt-depleted 100 Ma old mantle residues. Such high degree of partial melting is inconsistent with the low degree (1–5%) of partial melting inferred from heavy REE of type I peridotites (Fig. 7). Along the 1.2 Ga curve, type I peridotites correspond to 2–4% melt-depleted residues. A Proterozoic mantle age is also reflected by Hf isotope data of some type I and type IIa clinopyroxenes (Table 5). In particular, clinopyroxenes from type IIa peridotites have distinctly high ε_{Hf} at given ε_{Nd}, well above the OIB and MORB fields (Fig. 8b). These samples can therefore not be generated recently from a convecting asthenospheric mantle, but must have been produced by an ancient partial melting event (Fig. 11b). Hf model ages for type I and type IIa peridotites range from 0.9 to 3.6 Ga (with two unrealistic estimates, Table 5) and most of them are between 0.9 and 2.1 Ga, consistent with a Proterozoic mantle. Nevertheless, it appears that the Hf model ages are higher than the Nd model ages (Table 5). This can partly be explained by the fact that Hf is less affected than Nd by metasomatism (Fig. 7, and see the next section), due to the lower incompatibility of Sm and Nd compared to Lu and Hf.

To sum up, data available suggest that the studied peridotites are likely derived from a Proterozoic SCLM, a conclusion also supported by the Os isotopic data (Wu et al., 2003; Zhou et al., 2007). On the basis of Os isotopic analyses, Wu et al. (2003) suggested that the SCLM beneath Shuangliao might be variable in age from Proterozoic to Phanerozoic. While the Proterozoic mantle is evidenced from Nd and Hf isotopes compositions of type I and IIa peridotites, the age for type IIb peridotites remains to assess. In principle, a Phanerozoic mantle would exhibit isotopes similar to those of the convective mantle (defined by oceanic basalts including MORB and OIB). The isotopic composition of type IIb peridotites is within or proximal to the MORB and OIB field (Fig. 11). This implies that type IIb peridotites either were derived from a young lithospheric mantle or represent an ancient mantle whose isotopic composition has been seriously overprinted by metasomatising melts. It is difficult to distinguish between these models, but unrealistically high volume of melts required in the ancient mantle model makes us favor the model involving a young mantle (see next section).

5.2. Behavior of Sm–Nd and Lu–Hf pervasive metasomatism

Two different mechanisms of metasomatism have been proposed to interpret the geochemical characteristics of peridotites. "Wall-rock" metasomatism is related to melt transport in fractures forming veins and dykes and is considered a local phenomenon. Compositional and textural changes due to interaction with melts from fractures are generally confined to wall-rocks (Kempton, 1987). In this model, modally metasomatized peridotites generally occur adjacent to vein conduits, whereas cryptically metasomatized peridotites are more distant (Menzies et al., 1985). The wall-rock peridotites adjacent to veins are generally characterized by convex-upward or flat

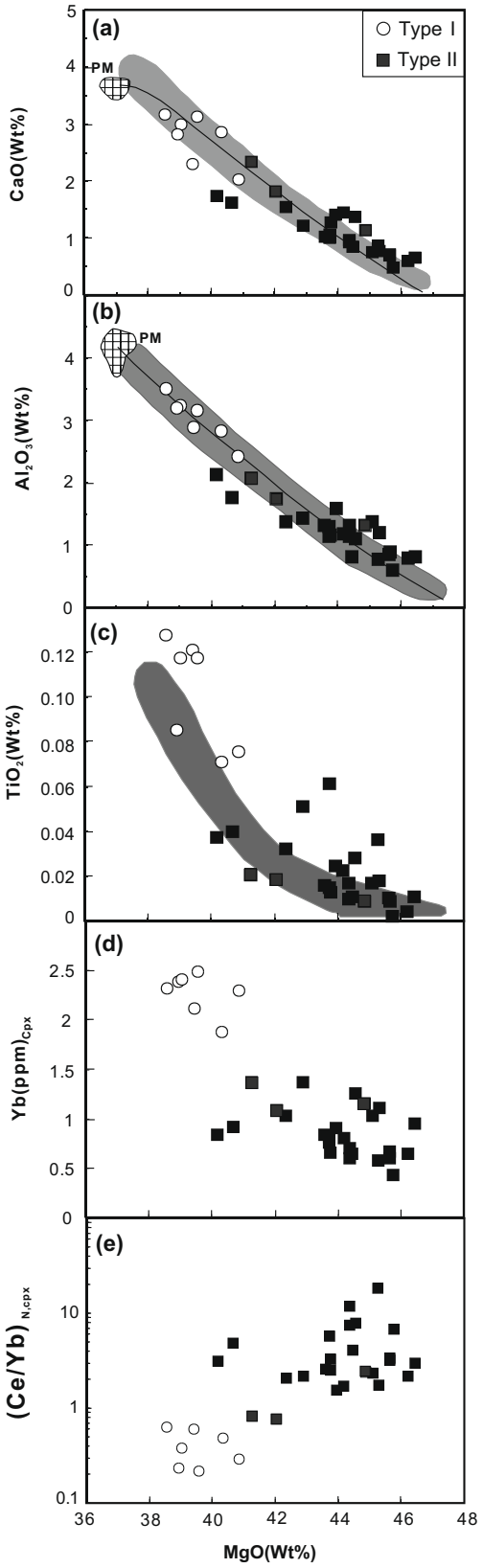

Fig. 5. (a–c). Plots of CaO, Al_2O_3 and TiO_2 against MgO for peridotite xenoliths from Shuangliao and Jiaohe. The shaded fields represent the compositional range for worldwide peridotites (Takazawa et al., 2000, and references therein). Black line is near-fractional melting model trend of a starting source of primitive spinel peridotites using the model of Niu (1997). Primitive mantle compositions are after Hart and Zindler (1986). (d–e) Plots of Yb and $(Ce/Yb)_n$ in clinopyroxene versus whole rock MgO contents. Ce/Yb ratios are normalized to chondrite value (Sun and McDonough, 1989).

REE patterns and Fe-enrichment. Another mechanism of metasomatism corresponds to melt migration by percolation along grain boundaries in a solid matrix (i.e., porous flow). In this model, the reactional surface is nearly unlimited; therefore infiltrated melt is likely to interact more strongly (Navon and Stolper, 1987). The metasomatic agent involved is generally a small melt fraction rich in volatiles. Such melts are believed to have low viscosities and solidification temperatures and are able to pervasively infiltrate large volumes of relatively cold lithospheric peridotites (McKenzie, 1989; Kelemen et al., 1995; Bedini et al., 1997; Xu and Bodinier, 2004). Such a diffuse metasomatism is generally characterized by a lack of Fe-enrichment and highly fractionated REE patterns ranging from U-shaped to steadily enriched patterns (Bodinier et al., 1990; Bedini et al., 1997; Ionov and Harmer, 2002). It is now widely accepted that selective enrichment of incompatible elements in many peridotites can be accounted for by chromatographic processes, such as proposed by Navon and Stolper (1987).

Most of the refractory peridotites from Shuangliao and Jiaohe show sign of metasomatic enrichment in incompatible elements (Fig. 7). There is no evidence for metasomatism-induced petrographic change, as the variation in mode of olivine and clinopyroxene is well correlated with $Cr\#_{sp}$ (Fig. 4a). Therefore, the metasomatism that was responsible for the enrichment of incompatible elements in the Shuangliao and Jiaohe peridotites is largely cryptic, i.e., only introducing incompatible elements without any petrographic modification (Frey and Green, 1974). Lack of Fe-enrichment (Fig. 4b) is not consistent with wall-rock metasomatism. Instead, extremely variable LREE enrichment and almost constant HREE observed in the cpx studied in this paper (Fig. 7) are virtually the same as those predicted by Navon and Stolper's (1987) chromatographic model, thus confirming the important role of chromatographic metasomatism in the mantle beneath Northeast China. We regard silicate melt as a metasomatic agent given the volatile-rich silicate glass observed in BLS-2 (Yu et al., 2007b).

Comparison of the variation of Sm, Nd, Hf and Lu in cpx with the modeled variation of melting residues (Fig. 6) suggests that Hf contents (<0.5 ppm) in type IIa peridotites are either not or only slightly affected by metasomatic processes, whereas Nd content in cpx is significantly altered by metasomatism (Fig. 6c and d). On the other hand, both Hf and Nd in type IIb peridotites plot markedly off the depletion trend, suggesting the severe modification of these elements during metasomatism. These geochemical features of type IIa and type IIb clinopyroxenes can be explained by chromatographic metasomatism, in which elements move through porous peridotites at rates that are inversely proportional to their solid-melt partition coefficients (Navon and Stolper, 1987). The enrichment front of the strongly incompatible elements thus moves faster than that of less incompatible elements. In the peridotite-melt system, the incompatibility of these four concerned elements varies in the following order: Nd > Sm > Hf > Lu. Because Nd migrates faster than Hf during pervasive percolation, it is possible to generate type IIa clinopyroxenes with strong Nd enrichment but weak to moderate Hf enrichment. When a sample is affected by fronts of both Hf and Nd, it shows trace element signature similar to those for type IIb peridotites.

5.3. Nd–Hf isotopic decoupling as a result of chromatographic metasomatism

Because of similar geochemical characteristics of the Lu–Hf and Sm–Nd systematics, Nd–Hf isotope compositions are commonly correlated. This is highlighted by oceanic basalts including MORB and OIB, defining the mantle array in the Nd–Hf isotope space (Nowell et al., 1998). However, a number of studies of mantle peridotites have shown very high $^{176}Hf/^{177}Hf$ in clinopyroxene, garnet or whole-rocks at moderate Nd isotope ratios, making some samples plotting well above the mantle Hf–Nd array (Salters and Zindler, 1995; Schmidberger et al., 2002; Bizimis et al., 2003; Aulbach et al., 2004; Bedini et al., 2004; Carlson et al., 2004; Ionov et al., 2005, 2006; Wu et al., 2006; Choi et al., 2007; Bianchini et al., 2007; Simon et al., 2007). This phenomenon is also observed for some samples from Shuangliao and Jiaohe (Fig. 8b).

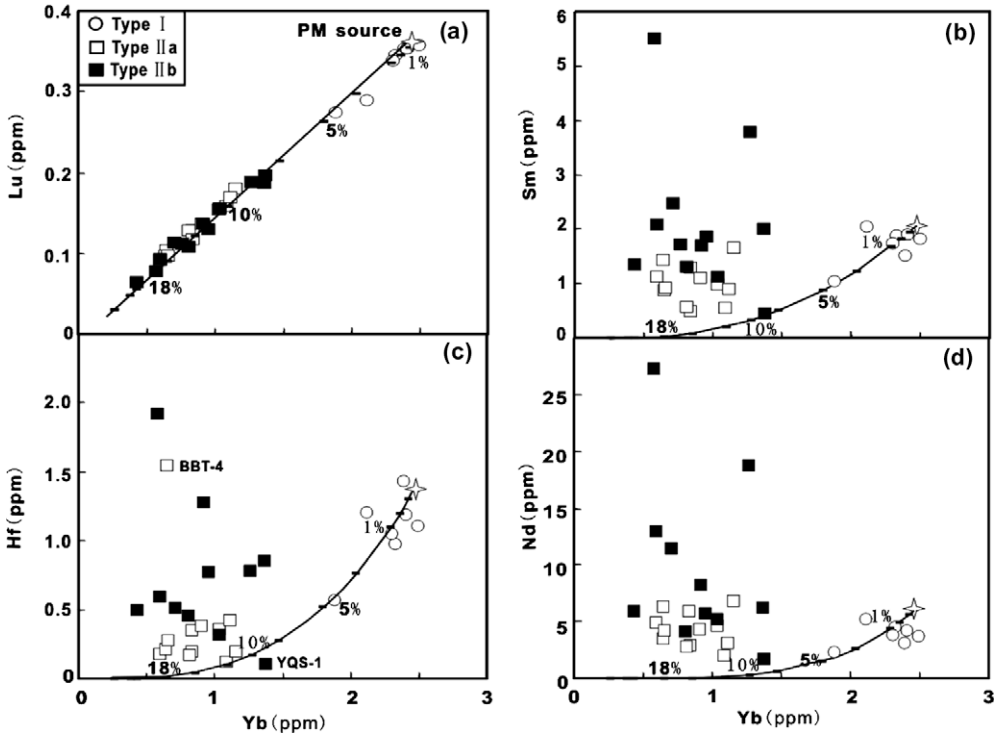

Fig. 6. REE and trace element abundances of cpx from Shuangliao and Jiaohe peridotites. Normalisation values are from Sun and McDonough (1989).

Models that have been proposed to account for the Nd–Hf isotope decoupling in the mantle lithosphere can be grouped into three categories: (a) mantle melting in the presence of garnet (Schmidberger et al., 2002; Ionov et al., 2005); (b) high degree of partial

Table 4
Trace element concentration (ppm) in clinopyroxenes from Shuangliao and Jiaohe peridotites.

	BBT-8	BLS-1	BLS-3	BLS-5	NBS-1	YQS-7	YQS-9	BBT-1	BBT-2	BBT-4	BBT-5	BBT-7	BLS-6	YQS-5	YQS-6	YQS-8
	Type I							Type II a								
Yb	2.11	2.39	2.49	2.32	1.88	2.30	2.41	0.84	0.60	0.64	0.64	1.03	0.65	1.09	1.15	0.81
Sc	45.97	53.21	27.42	48.92	53.87	66.25	62.64	42.98	70.05	77.57	58.47	49.63	62.15	68.54	77.37	85.34
Ti	2511	1876	2294	2261	1630	2428	3184	576	432	395	369	600	366	670	517	372
V	215	274	275	261	252	290	298	224	216	229	211	188	211	241	253	281
Cr	5298	4470	4899	4557	4404	5671	5294	6216	7980	8481	8276	6732	6705	5028	7086	8846
Mn	664	605	595	661	552	580	591	676	548	519	542	645	541	553	569	567
Co	29.23	24.49	21.39	27.40	23.61	31.72	25.48	40.67	27.76	22.67	24.78	25.60	23.18	24.17	25.22	20.61
Ni	401	351	345	339	372	337	323	621	492	397	409	403	429	388	366	335
Ga	4.26	3.02	3.07	3.93	2.81	3.18	3.43	2.84	1.54	1.52	1.59	2.41	1.65	1.70	1.68	2.01
Rb	0.13	0.12	0.10	0.16	0.12	0.07	0.05	0.38	0.51	0.17	0.98	0.15	0.04	0.06	0.09	0.03
Sr	67.77	23.61	50.27	44.29	48.34	39.71	59.36	80.97	120.60	79.78	132.60	86.57	100.60	37.78	53.77	73.65
Y	19.71	20.33	21.85	21.21	15.81	21.04	21.89	7.06	5.46	5.08	6.30	8.48	4.57	8.84	9.92	5.85
Zr	29.62	38.91	28.25	22.25	9.38	30.04	31.34	5.43	8.14	53.42	9.99	15.97	9.95	5.47	5.41	6.02
Nb	0.27	0.23	0.09	1.56	0.85	0.10	0.28	2.08	1.27	1.00	1.14	0.66	1.36	0.46	0.68	0.97
Hf	1.21	1.43	1.11	0.98	0.57	1.05	1.19	0.19	0.18	1.55	0.21	0.36	0.27	0.12	0.20	0.17
Ta	0.03	0.09	0.02	0.16	0.09	0.01	0.07	0.25	0.14	0.20	0.16	0.08	0.12	0.04	0.02	0.08
Pb	0.60	4.62	0.90	2.20	0.83	1.45	1.45	1.16	1.65	2.74	2.28	1.36	2.17	1.43	1.82	1.39
Th	0.06	0.07	0.02	0.29	0.07	0.01	0.02	0.64	0.12	0.18	0.18	0.22	0.72	0.07	0.08	0.33
U	0.02	0.22	0.03	0.09	0.03	0.02	0.02	0.18	0.04	0.26	0.07	0.07	0.19	0.03	0.03	0.10
Ba	1.62	1.25	0.16	1.69	0.25	0.33	0.13	0.87	1.65	0.85	2.25	0.44	0.22	0.11	0.32	0.11
La	1.37	0.55	0.38	2.68	1.55	0.48	0.86	5.88	2.74	2.04	3.62	3.12	3.74	1.27	3.30	4.15
Ce	4.57	2.02	1.94	5.30	3.29	2.41	3.26	9.42	7.30	5.09	9.38	7.75	7.64	3.02	9.84	7.24
Pr	0.89	0.45	0.51	0.80	0.43	0.57	0.69	0.89	1.07	0.77	1.38	1.07	0.99	0.42	1.51	0.75
Nd	5.26	3.11	3.69	4.52	2.27	3.80	4.25	2.87	4.91	3.54	6.28	4.63	4.19	1.96	6.80	2.79
Sm	2.05	1.52	1.83	1.87	1.04	1.73	1.91	0.49	1.13	0.88	1.44	0.98	0.91	0.55	1.65	0.58
Eu	0.81	0.61	0.76	0.75	0.47	0.71	0.77	0.18	0.39	0.31	0.49	0.32	0.30	0.21	0.47	0.24
Gd	3.15	2.78	3.25	3.17	2.08	2.96	3.14	0.66	1.07	0.91	1.37	1.14	0.86	0.89	1.56	0.69
Tb	0.62	0.56	0.65	0.60	0.44	0.59	0.62	0.15	0.18	0.16	0.24	0.22	0.14	0.19	0.27	0.14
Dy	3.88	3.83	4.17	4.01	2.99	3.73	4.03	1.11	1.03	0.94	1.27	1.50	0.86	1.41	1.74	0.94
Ho	0.81	0.84	0.88	0.83	0.64	0.79	0.84	0.26	0.20	0.19	0.24	0.34	0.18	0.33	0.36	0.22
Er	2.24	2.45	2.51	2.41	1.92	2.34	2.53	0.82	0.59	0.55	0.68	1.01	0.56	1.05	1.10	0.71
Tm	0.33	0.37	0.39	0.37	0.29	0.36	0.37	0.13	0.09	0.09	0.10	0.16	0.09	0.16	0.17	0.12
Lu	0.29	0.35	0.36	0.35	0.27	0.34	0.35	0.13	0.09	0.09	0.10	0.10	0.15	0.10	0.16	0.18	0.13

	YQS-11	YQS-12	YQS-16	BBT-6	BBT-9	BBT-10	BBT-11	BLS-2	YQS-1	YQS-2	YQS-3	YQS-4	YQS-10	YQS-14	YQS-15
	Type IIa			Type IIb											
Yb	0.83	0.90	1.11	0.76	0.58	1.37	0.91	0.95	1.37	0.43	1.04	0.60	0.81	0.71	1.26
Sc	60.65	55.24	71.93	43.92	48.67	47.55	13.56	71.99	77.04	127.70	77.55	84.68	74.70	73.00	91.02
Ti	538	639	849	671	939	1096	591	475	728	286	748	495	643	398	924
V	234	236	263	222	156	222	200	231	241	282	235	252	236	192	281
Cr	8280	7009	8128	8195	9813	8688	6398	10594	4327	9978	5291	7889	7149	6943	8918
Mn	499	593	577	591	572	600	632	537	543	544	540	518	530	538	510
Co	23.54	24.67	24.27	27.77	29.10	28.41	31.15	31.28	19.15	23.62	20.94	20.07	23.99	23.12	22.74
Ni	327	402	388	426	490	437	533	542	300	392	339	312	387	386	422
Ga	1.97	2.02	2.24	2.68	2.02	2.46	2.41	1.87	1.79	1.38	1.70	1.87	1.56	1.64	2.00
Rb	0.05	0.04	0.05	1.01	0.60	0.88	0.52	0.20	0.01	0.12	0.05	0.07	0.09	0.15	0.27
Sr	69.08	40.98	87.97	173.30	444.20	116.10	145.70	141.10	37.13	85.70	89.39	230.90	59.48	166.60	290.70
Y	7.23	7.74	9.80	6.74	9.08	13.88	6.91	10.37	11.35	5.24	8.51	5.02	9.31	7.12	12.55
Zr	10.99	12.41	12.11	30.77	55.82	19.72	48.57	42.01	3.62	19.80	13.34	55.28	11.68	21.74	15.70
Nb	0.77	0.35	0.50	3.58	1.32	2.33	1.96	0.86	0.39	0.65	0.39	0.25	1.02	2.73	0.60
Hf	0.35	0.38	0.43	0.77	1.92	0.86	1.28	0.78	0.11	0.50	0.32	0.59	0.45	0.51	0.78
Ta	0.06	0.03	0.03	0.41	0.19	0.12	0.22	0.09	0.05	0.09	0.08	0.03	0.05	0.22	0.03
Pb	0.93	0.76	1.10	1.41	1.89	2.17	2.55	1.62	0.80	1.47	1.66	2.02	1.14	1.82	1.52
Th	0.11	0.03	0.32	1.29	1.67	1.28	1.55	1.59	0.09	0.89	0.28	0.29	0.05	0.35	0.48
U	0.04	0.02	0.08	0.30	0.34	0.32	0.50	0.44	0.04	0.06	0.08	0.10	0.03	0.09	0.08
Ba	0.15	0.07	0.15	12.50	2.08	7.94	2.99	0.37	1.03	0.48	0.14	0.27	0.14	1.68	1.54
La	2.51	1.52	4.46	9.09	16.71	7.47	8.35	3.95	1.88	4.80	3.59	10.02	1.62	7.80	14.89
Ce	7.72	5.03	6.93	15.77	38.01	10.60	15.96	10.12	4.04	10.41	8.62	25.33	4.93	18.84	35.38
Pr	1.19	0.86	0.74	1.93	5.71	1.27	2.01	1.38	0.45	1.39	1.19	3.37	0.80	2.57	4.58
Nd	5.96	4.32	3.07	7.98	27.25	6.26	8.18	5.77	1.74	5.88	5.19	12.91	4.12	11.47	18.73
Sm	1.29	1.10	0.89	1.72	5.50	2.01	1.71	1.87	0.46	1.34	1.14	2.08	1.31	2.48	3.78
Eu	0.43	0.35	0.37	0.56	1.54	0.72	0.51	0.75	0.19	0.43	0.36	0.62	0.50	0.80	1.24
Gd	1.25	1.22	1.36	1.62	4.26	2.62	1.47	2.43	0.95	1.28	1.21	1.21	1.84	2.13	3.08
Tb	0.23	0.23	0.27	0.24	0.58	0.47	0.23	0.42	0.23	0.21	0.23	0.21	0.33	0.31	0.52
Dy	1.37	1.40	1.79	1.35	2.52	2.81	1.36	2.30	1.76	1.10	1.46	1.03	1.92	1.60	2.67
Ho	0.28	0.30	0.38	0.25	0.37	0.57	0.28	0.43	0.40	0.20	0.31	0.18	0.37	0.28	0.49
Er	0.82	0.90	1.14	0.78	0.90	1.54	0.84	1.13	1.32	0.50	0.97	0.56	0.98	0.75	1.37
Tm	0.12	0.14	0.18	0.12	0.10	0.22	0.13	0.15	0.21	0.07	0.15	0.09	0.13	0.11	0.19
Lu	0.12	0.14	0.17	0.11	0.08	0.19	0.14	0.13	0.20	0.06	0.16	0.09	0.11	0.11	0.19

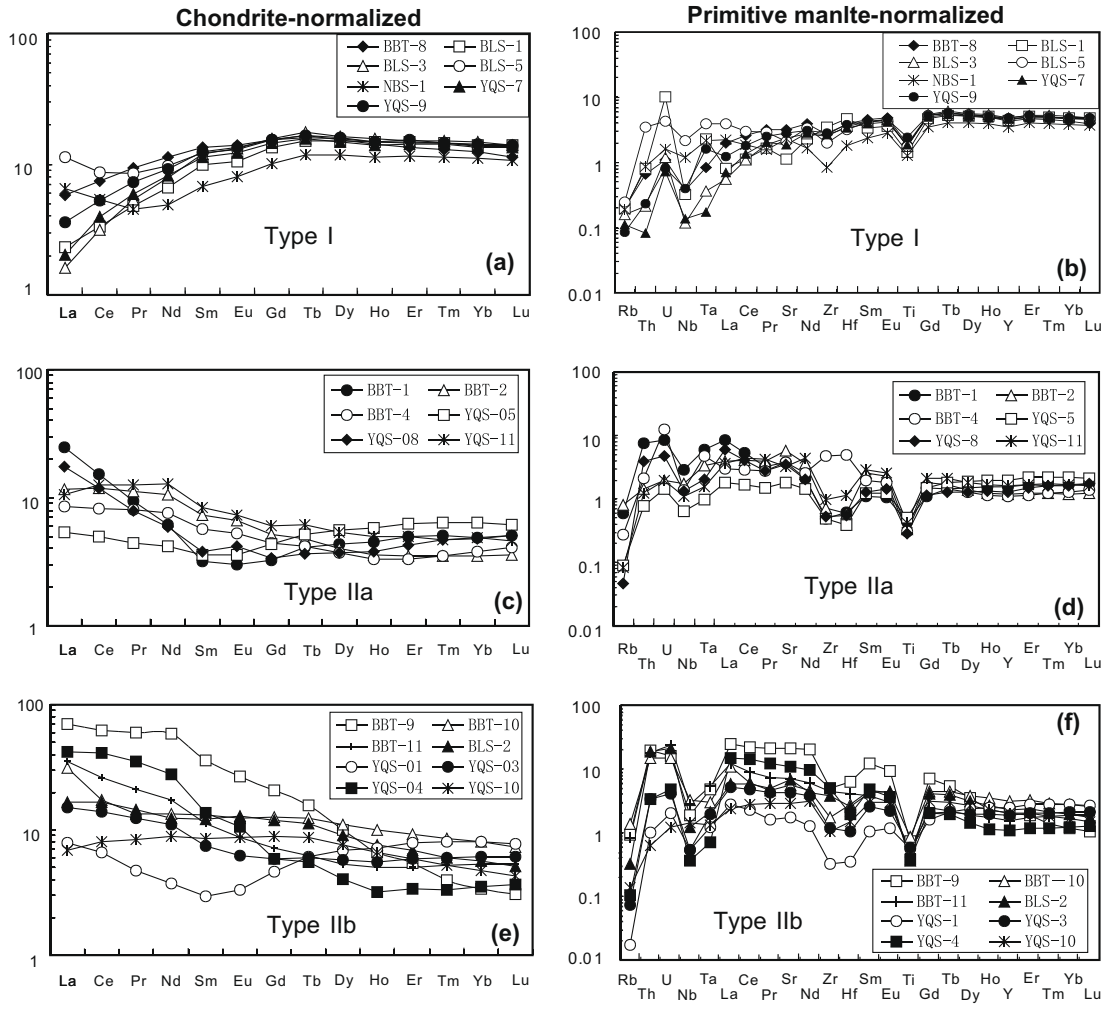

Fig. 7. Yb content vs. (a) Lu, (b) Sm, (c) Hf, and (d) Nd concentrations in cpx. Solid lines show elemental variation in residues left by fractional partial melting of a hypothesized primitive mantle (Sun and Mcdonough, 1989). Star represents the starting point of partial melting curve. Melting model is after Johnson et al. (1990). Parameters are listed in Table 5.

Table 5
Sr–Nd–Hf isotope compositions in clinopyroxenes from Shuangliao and Jiaohe peridotites.

Sample	$^{87}Rb/^{86}Sr$	$^{87}Sr/^{86}Sr$	$^{147}Sm/^{144}Nd$	$^{143}Nd/^{144}Nd$	ε Nd (t)	T_{Nd} (Ma)	$^{176}Lu/^{177}Hf$	$^{176}Hf/^{177}Hf$	ε Hf (t)	T_{Hf} (Ma)
Type I										
BLS-1	0.0152	0.703065 ± 15	0.2951	0.513482 ± 11	16.0	1307	0.0352	0.283413 ± 11	22.6	15113
BLS-3	0.0058	0.702791 ± 14					0.0459	0.283248 ± 9	16.5	1980
BLS-5	0.0103	0.703092 ± 14	0.2508	0.513251 ± 12	11.7	1725	0.0500	0.283277 ± 8	17.4	1586
YQS-9	0.0026	0.702649 ± 14	0.2717	0.513377 ± 8	14.0	1500	0.0421	0.283398 ± 17	21.9	3640
Type IIa										
BBT-1	0.0136	0.703806 ± 14	0.1035	0.512917 ± 9	5.9	Future	0.0945	0.284394 ± 25	55.7	1399
BBT-2	0.0121	0.703771 ± 10	0.1386	0.512878 ± 9	5.0	Future	0.0706	0.284275 ± 26	52.2	2108
BBT-4	0.0063	0.703746 ± 14	0.1495	0.512891 ± 10	5.2	Future	0.0095	0.284423 ± 35	59.0	Future
YQS-8	0.0012	0.702979 ±10	0.1260	0.513049 ± 10	8.4	Future	0.1066	0.284082 ± 14	44.4	948
YQS-11	0.0022	0.703840 ± 11	0.1311	0.512556 ± 8	-1.3	191	0.0480	0.284588 ± 14	63.8	6183
Type IIb										
BBT-9	0.0039	0.704923 ± 11	0.1220	0.512791 ± 9	3.4	Future	0.0058	0.282974 ± 7	7.9	Future
BBT-10	0.0220	0.703923 ± 13					0.0310	0.283175 ± 8	14.3	Future
BBT-11	0.0103	0.703740 ± 14	0.1261	0.512858 ± 13	4.6	Future	0.0151	0.283101 ± 16	12.1	Future
BLS-2	0.0041	0.703506 ± 13	0.1955	0.512941 ± 11	5.9	Future	0.0238	0.283060 ± 18	10.4	Future
YQS-1	0.0009	0.705219 ± 13	0.1584	0.512837 ± 9	4.1	Future	0.2602	0.283272 ± 8	11.7	118
YQS-3	0.0015	0.704967 ± 10	0.1324	0.512749 ± 7	2.5	Future	0.0695	0.283254 ± 15	16.1	707
YQS-4	0.0008	0.707004 ± 13	0.0975	0.512579 ± 9	-0.7	92	0.0223	0.283138 ± 17	13.2	Future
YQS-10	0.0042	0.703143 ± 13	0.1919	0.513082 ± 9	8.7	Future	0.0339	0.283453 ± 13	24.1	34885

Model ages in Ma calculated using Sm–Nd and Lu–Hf data from Table 3 and this table. Future model ages are enclosed in parentheses.
Model ages were calculated assuming a linear isotopic evolution for Nd and Hf using the following parameters: $\lambda^{147}Sm = 6.54 \times 10^{-12}\ yr^{-1}$, $\lambda^{176}Lu = 1.867 \times 10^{-11}\ yr^{-1}$, present day Bulk Earth values are $^{147}Sm/^{144}Nd = 0.1967$, $^{143}Nd/^{144}Nd = 0.512638$; $^{176}Lu/^{177}Hf = 0.0332$ and $^{176}Hf/^{177}Hf = 0.282772$.

melting; (c) melt–mantle interaction (Salters and Zindler, 1995; Bizimis et al., 2003) or metasomatism involving different metasomatizing agents (Wittig et al., 2007).

The first model involves the presence of garnet during mantle melting (Schmidberger et al., 2002; Ionov et al., 2005). Because garnet preferentially incorporates Lu relative to Hf, to a greater extent than Sm relative to Nd, mantle melting in the presence of garnet will lead to a significant fractionation of Lu/Hf and Sm/Nd ratios (Schmidberger et al., 2002). Mantle domains with high Lu/Hf and radiogenic Hf isotope compositions can equally be created by HREE redistribution related to spinel-garnet phase transition (Ionov et al., 2005). The high Lu/Hf ratios in those rocks are not matched by correspondingly high Sm/Nd. Over time, they will develop radiogenic Hf isotope compositions, which will not be matched by equally radiogenic Nd isotope signatures. This model predicts (a) a more significant depletion in MREE relative to HREE (Xu et al., 2002; Wittig et al., 2007) and/or (b) characteristic texture such as spinel–pyroxene clusters that is indicative of precursor garnet (Nicolas et al., 1987). Unfortunately, these two features are not observed in the Shuangliao and Jiaohe case. It is noted that trace element composition is somehow correlated with the isotopes for the Shuangliao and Jiaohe peridotites (Fig. 9). Specifically, type IIa peridotites show non-radiogenic Nd and radiogenic Hf isotopic ratios ($\varepsilon_{Nd} = -1.3$ to 8.4, $\varepsilon_{Hf} = 44.4–63.8$) (Fig. 8b), plotting markedly off the mantle array. Type IIb peridotites have relatively non-radiogenic Nd and Hf ($\varepsilon_{Nd} = -0.7$ to 8.7, $\varepsilon_{Hf} = 7.9–24$) and plot within or proximal to the mantle array. Such an isotopic composition is not consistent with their refractory character, but is in agreement with the enrichment of incompatible elements, indicating resetting of both Nd and Hf isotopes by metasomatic enrichment.

To evaluate the effect of melting degree and ages of the lithospheric mantle on Nd–Hf isotopic systematics, ε_{Nd} and ε_{Hf} for mantle residues of different ages are calculated (Fig. 11a). In general, Hf–Nd isotope compositions of mantle residues fall along the mantle array and its extension in the Nd–Hf isotopic space, likely due to progressively higher Lu/Hf and Sm/Nd ratios during an increasing degree of partial melting as Hf and Nd are more incompatible than Lu and Sm in peridotites (Bizimis et al., 2003). Specifically, fertile peridotites (melting degree < 5%) of young age (100 Ma) are plotted within the OIB–MORB field, whereas refractory peridotites (melting degree > 10%) plot outside of the OIB–MORB field (Fig. 11a). The Nd–Hf isotopic evolution trend for a young mantle (~100 Ma) is steeper than that for older mantle. Long-term residence in the lithosphere allows for the development of extreme Hf (and Nd) isotopic compositions (Fig. 11a). However, the absolute ε_{Hf} and ε_{Nd} values are less extreme for the young mantle relative to the old one. The melting degree estimated for type II peridotites ranges from 8% to 18% (Fig. 6a), corresponding to ε_{Hf} of 100–600 if 1.2 Ga elapsed since the melting event. Given that

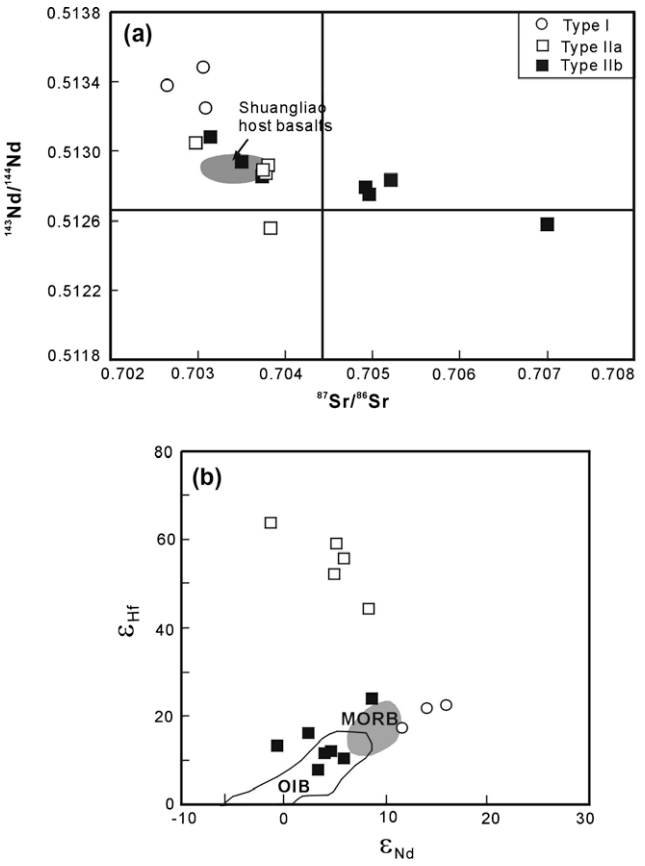

Fig. 8. Sr–Nd–Hf isotope compositions in clinopyroxene seperates from Shuangliao and Jiaohe peridotites. Sr–Nd isotope data of Shuangliao host basalts and ocean island basalt (OIB) field are from Zhang (2006) and Zindler and Hart (1986), respectively. Nd–Hf isotope composition range of mid-ocean ridge basalt (MORB) and OIB are after Nowell et al. (1998).

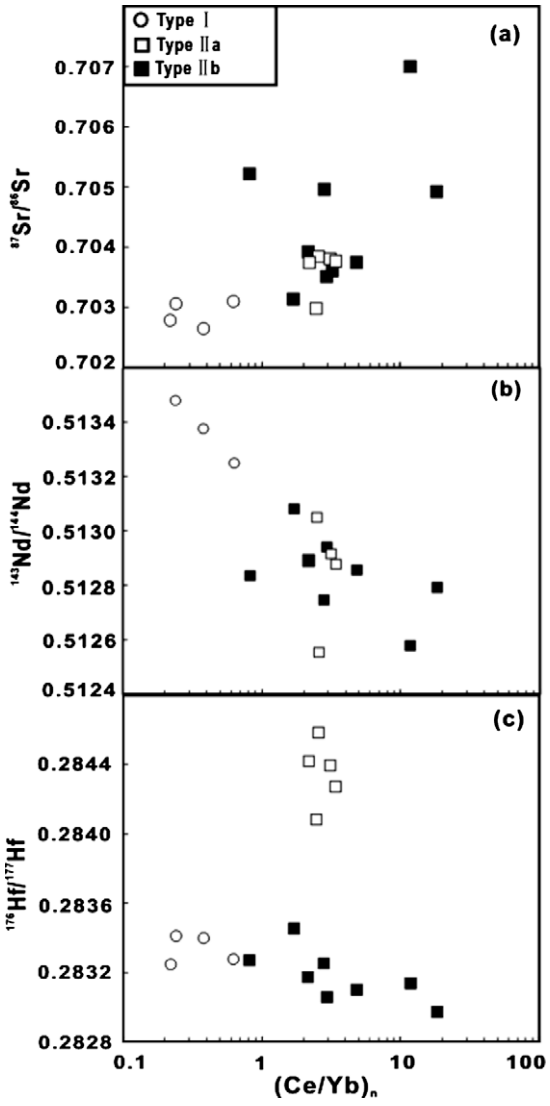

Fig. 9. Correlations of Sr–Nd–Hf isotopes versus $(Ce/Yb)_n$ in clinopyroxenes from Shuangliao and Jiaohe peridotites. Sr and Nd isotopes of cpx show good correlations with $(Ce/Yb)_n$, but Hf isotope display a more complicated character.

the observed ε_{Hf} for type II peridotites is lower than 80, the Nd–Hf isotopic decoupling cannot be simply due to degrees of partial melting. It is possible that both ε_{Hf} and ε_{Nd} may have been lowered during a process other than partial melting.

The third model calls for melt–mantle interaction (Salters and Zindler, 1995; Bizimis et al., 2003) or metasomatism involving different metasomatic agents (Wittig et al., 2007) to account for variable radiogenic Hf at a near constant Nd isotope composition. Metasomatism is assumed to affect mainly Nd isotope compositions, but not so much Hf isotopes because of higher mobility of Nd relative to Hf in mantle fluids (Bizimis et al., 2003; Bedini et al., 2004). The ubiquitous metasomatic signature in type II peridotites from Shuangliao and Jiaohe renders this model likely. It remains to assess whether the Hf–Nd isotopic decoupling was related to chromatographic metasomatism with a single agent, or multiple metasomatism involving different metasomatizing agents.

Wittig et al. (2007) recently attributed the two groups of peridotite xenoliths from French Massif Central (FMC) to metasomatism involving different metasomatic agents. Specifically, clinopyroxenes from northern FMC characterized by unaffected Zr, Hf, Th abundances and decoupling Nd–Hf isotope compositions are considered to be metasomatized by hydrous or carbonatitic agents. Such agents have high mineral/liquid partition coefficients for heavy REE and HFSE (Klemme et al., 1995; Sweeney et al., 1995). Thus, Lu and Hf concentrations are low in hydrous and carbonatitic agents. In contrast, cpx from southern FMC are marked by overall incompatible trace element enrichment in Zr, Hf and Th abundances and relatively less radiogenic Hf, which is attributed to having been overprinted by silicate melt metasomatism. Although such a multiple metasomatism model is attractive, we favor a chromatographic model for the Shuangliao and Jiaohe case for the following reasons: (a) The two sub-groups show essentially a similar trace element signature. Their difference is only the extent of enrichment. (b) The Nd isotopic composition of type IIa and type IIb clinopyroxenes is essentially similar. The distinct Hf isotopes between these two groups is consistent with trace element evidence that Hf in type IIa peridotites remains intact or only slightly altered, in contrast to the severe modification of Nd. (c) Similar equilibrium temperatures suggest that the two groups are not spatially distinct. Silicate melt is expected to produce enrichments in most incompatible elements including Lu and Hf, so it is likely to be responsible for the incompatible trace element enrichment and resetting of Lu–Hf and Sm–Nd isotope systematics observed in the Shuangliao and Jiaohe peridotites.

In order to further constrain this model, we modeled Sm–Nd and Lu–Hf concentration and isotopic variation of melt depletions followed by recent metasomatism (Fig. 11b and c). For the studied peridotites, both 100 Ma and 1.2 Ga old depleted peridotites left after various degrees of partial melting are used in the binary mixing. The metasomatic agent is a small silicate melt fraction with 'normal' Hf and Nd isotope compositions, i.e., from within the mantle array in Nd–Hf isotope space. The mixing lines in Fig. 11b and c are concave upwards because of the greater Nd/Hf ratio in the melt relative to that of a depleted peridotite. They significantly deviate from the terrestrial array, thus accounting for the observed Nd–Hf isotopic decoupling (Fig 11b and c). The percentage of melt addition required to generate the isotopic composition of type IIa peridotites is lower than that for type IIb peridotites, broadly consistent with the fact that the extent of metasomatism experienced by type IIa peridotites is lower than that for type IIb peridotites.

When a 1.2 Ga lithospheric mantle is involved, the percent of melt addition for type IIa peridotites ranges between 5% and 6% for 8% and 18% melt-depleted residues. These estimates are reasonable and are consistent with the melting degree constrained by trace element data (Fig. 7). However, for a 100 Ma lithospheric mantle, residues of higher degree (>15%) are required. Again, these argue for a Proterozoic mantle for type IIa peridotites. Another point that needs explaining is the apparent negative correlation of type IIa peridotites in the Nd–Hf isotopic space (Fig. 11b). For instance, sample YQS-11 has the lowest ε_{Nd} of −1.3 but the highest ε_{Hf} of 64, whereas YQS-8 displays the highest ε_{Nd} of 8.4 but the lowest ε_{Hf} of 44. Whether this correlation is true remains to be assessed when additional data become available. It can be attributed to chromatographic metasomatism of residues with variable degree of melt depletion and time-integrated effect of various enrichment events. As illustrated in Fig. 7, the enrichment of incompatible elements is more pronounced in refractory peridotites than in fertile peridotites. If the enrichment associated with the refractory peridotites (higher ε_{Hf}) took place earlier than for less refractory samples (lower ε_{Hf}), the former will develop with time a negative ε_{Nd} while keeping a relatively high ε_{Hf} given the higher incompatibility of Nd relative to Hf.

Type IIb peridotites display lower ε_{Hf} and ε_{Nd} compared to type IIa peridotites, thus requiring a higher percentage of melt addition (Fig. 11b and c). The age of type IIb peridotites is difficult to assess, because of significant modification of their isotopic signature by melt percolation processes. Nevertheless, mixing calculation between melt and peridotites yields some constraints on the age of type IIb peridotites. Fig. 11b shows that the Nd–Hf isotopic systematics of type IIb peridotites can be accounted for by interaction between melts and a <8% melt-depleted 1.2 Ga residue. This hypothesized fertile-moderately refractory component is inconsistent with the refractory characteristics of type IIb peridotites. Such

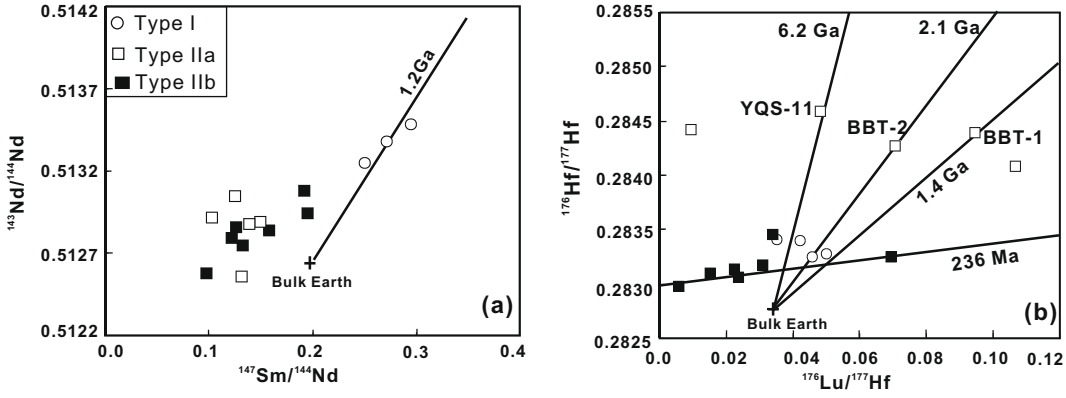

Fig. 10. (a) $^{143}Nd/^{144}Nd$ versus $^{147}Sm/^{144}Nd$ isotopic evolution diagram. Sm–Nd ages are calculated with $\lambda = 6.54 \times 10^{-12}$ and present day of Bulk Earth Values ($^{143}Nd/^{144}Nd = 0.512638$, $^{147}Sm/^{144}Nd = 0.1967$). (b) $^{176}Hf/^{177}Hf$ versus $^{176}Lu/^{177}Hf$ isotopic evolution diagram. Lu–Hf ages are calculated with $\lambda = 1.867 \times 10^{-11}$ and present day $^{176}Hf/^{177}Hf$ and $^{176}Lu/^{177}Hf$ of bulk earth are 0.282772 and 0.0332, respectively (Blichert-Toft and Albarède, 1997).

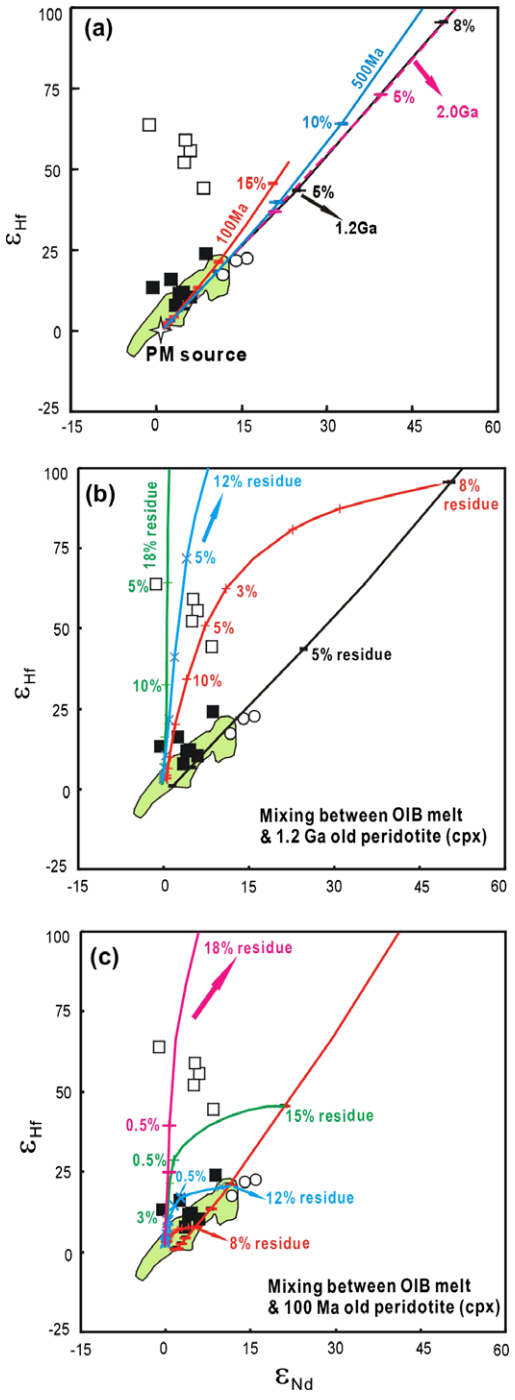

Fig. 11. (a) Calculated present-day Nd–Hf isotopic composition of residual peridotites of various melting degrees and ages. Ticks (%) on the cruves represent degree of partial melting from a primitive mantle source. (b) Binary mixing of a 1.2 Ga old cpx residues of variable degrees by an OIB-like melt. Two mixing lines are shown for comparison: OIB melt mixing with 8% and 18% melt-depleted 1.2 Ga old cpx. (c) Binary mixing of a 100 Ma old cpx residues of variable degrees by an OIB-like melt. Four mixing lines are shown for comparison: OIB melt mixing with 8%, 12%, 15% and 18% melt-depleted 100 Ma old cpx. Tick marks on the mixing lines in (b) and (c) show % of melt addition to cpx. The green area stands for MORB and OIB field (Stracke et al., 2003).

a problem can be overcome if a young mantle residue (100 Ma) is involved in mixing (Fig. 11c). In this sense, type IIb peridotites may have an age younger than type I and type IIa peridotites, although their precise formation age remains unknown.

6. Conclusions

The integration of mineralogy, major and trace element compositions and Sr–Nd–Hf isotope systematics of cpx from Shuangliao and Jiaohe peridotite xenoliths yields important implications about the nature of and processes within the mantle beneath Northeast China. The upper mantle beneath Shuangliao and Jiaohe consists of spinel lherzolite and harzburgite, with the abundance of harzburgite being more important in the xenolith population. Compositionally resembling the Group I peridotites from elsewhere, they are samples of the lithospheric mantle that has been subjected to variable degrees of partial melting (0–18%) and has been isolated from the convective mantle for ~1.3 Ga. Trace element and Sr–Nd–Hf isotopic data reveal extensive interaction between depleted mantle lithosphere and OIB-type silicate melts. Metasomatism, characterized by cryptic LILE-enrichment, is largely concentrated in refractory samples which can be further divided into two sub-types. Type IIa clinopyroxenes show Nd enrichment but no or weak Hf enrichment, and high radiogenic Hf isotope at moderate ε_{Nd} values (i.e., Nd–Hf isotope decoupling), whereas type IIb samples exhibit enrichment of both Nd and Hf and coupled Nd–Hf isotopes. Such a heterogeneous composition can be explained by chromatographic percolation of a refractory mantle by an asthenosphere-derived small silicate melt fraction.

Acknowledgements

We thank Fuyuan Wu, Kuo-Lung Wang, Tajana Rehfelt and Bor-Ming Jahn (editor in chief) for their constructive comments and suggestions that help improve the quality of the paper. We also thank Y. Liu, X.L. Tu, X.R. Liang and Y.H. Yang or technical assistance with diverse analyses. The authors gratefully acknowledge the financial support from the National Science Foundation of China (70914001; 40673038) and the CAS/SAFEA International Partnership Program for Creative Research Teams.

References

Aulbach, S., Griffin, W.L., O'Reilly, S.Y., McCandless, T.E., 2004. Genesis and evolution of the lithospheric mantle beneath the Buffalo Head Terrane, Alberta (Canada). Lithos 77, 413–451.

Bedini, R.M., Blichert-Toft, J., Boyet, M., Albarède, F., 2004. Isotopic constraints on the cooling of the continental lithosphere. Earth and Planetary Science Letters 223, 99–111.

Bedini, R.M., Bodinier, J.L., Dautria, J.M., Morten, L., 1997. Evolution of LILE-enriched small melt fractions in the lithospheric mantle: a case study from the East African Rift. Earth and Planetary Science Letters 153, 67–83.

Bertrand, P., Mercier, J.C., 1985. The mutual solubility of coexisting ortho- and clinopyroxene: toward an absolute geothermometer for the natural system? Earth and Planetary Science Letters 76, 109–122.

Bianchini, G., Beccaluva, L., Bonadiman, C., Nowell, G., Pearson, G., Siena, F., Wilson, M., 2007. Evidence of diverse depletion and metasomatic events in harzburgite–lherzolite mantle xenoliths from the Iberian plate (Olot, NE Spain): implications for lithosphere accretionary processes. Lithos 94, 25–45.

Bizimis, M., Sen, G., Salters, V.J.M., 2003. Hf–Nd isotope decoupling in the oceanic lithosphere: constraints from spinel peridotites from Oahu, Hawaii. Earth and Planetary Science Letters 217, 43–58.

Blichert-Toft, J., Albarède, F., 1997. The Lu–Hf isotope geochemistry of chondrites and the evolution of the mantle-crust system. Earth and Planetary Science Letters 148, 243–258.

Blichert-Toft, J., Chauvel, C., Albarède, F., 1997. Separation of Hf and Lu for high-precision isotope analysis of rock samples by magnetic sector-multiple collector ICP-MS. Contributions to Mineralogy and Petrology 127, 248–260.

Bodinier, J.L., Vasseur, G., Vernieres, J., Dupuy, C., Fabries, J., 1990. Mechanisms of mantle metasomatism: geochemical evidence from the Lherz Orogenic peridotite. Journal of Petrology 31, 597–628.

Carlson, R.W., Irving, A.J., Schulze Jr., D.J., Hearn, B.C., 2004. Timing of Precambrian melt depletion and Phanerozoic refertilization events in the lithospheric mantle of the Wyoming Craton and adjacent Central Plains Orogen. Lithos 77, 453–472.

Cabanes, N., Mercier, J.C.C., 1988. Insight into the upper mantle beneath an active extensional zone: the spinel-peridotite xenoliths from San Quintin (Baja California, Mexico). Contributions to Mineralogy and Petrology 100, 374–382.

Choi, S.H., Mukasa, S.B., Andronikov, A.V., Marcano, M.C., 2007. Extreme Sr–Nd–Pb–Hf isotopic compositions exhibited by the Tinaquillo peridotite massif,

Northern Venezuela: implications for geodynamic setting. Contributions to Mineralogy and Petrology 153, 443–463.
Downes, H., Dupuy, C., 1987. Textural, isotopic and REE variations in spinel peridotite xenoliths, Massif Central, France. Earth and Planetary Science Letters 82, 121–135.
E, M.L., Zhao, D.S., 1987. Cenozoic Basalts and their Deep-Seated Inclusions Eastern China, vol. 490. Scientific Press, Beijing.
Frey, F.A., Green, D.H., 1974. The mineralogy, geochemistry and origin of lherzolite inclusions in Victorian basanites. Geochimica et Cosmochimica Acta 38, 1023–1059.
Frey, F.A., Prinz, M., 1978. Ultramafic inclusions from San Carlos, Arizona: petrologic and geochemical data bearing on their petrogenesis. Earth and Planetary Science Letters 38, 129–176.
Frey, F.A., Suen, C.J., Stockman, H.W., 1985. The Ronda high temperature peridotite: geochemistry and petrogenesis. Geochimica et Cosmochimica Acta 49, 2469–2491.
Gao, S., Rudnick, R.L., Carlson, R.W., McDonough, W.F., 2002. Re–Os evidence for replacement of ancient mantle lithosphere beneath the North China craton. Earth and Planetary Science Letters 198, 307–322.
Griffin, W.L., O'Reilly, S.Y, Ryan, C.G., 1999. The composition and origin of subcontinental lithospheric mantle. In: Fei, Y. (Ed.), Mantle Petrology: Field Observations and High-Pressure Experimentation: A Tribute to Francis R. (Joe) Boyd, Houston, Texas, vol. 6. The Geochemical Society, Special Publication, pp. 13–43.
Hart, S.R., Zindler, A., 1986. In search of a bulk Earth composition. Chemical Geology 57, 247–267.
Ionov, D.A., Kramm, U., Stosch, H.G., 1992. Evolution of the upper mantle beneath the southern Baikal rift zone: an Sr–Nd isotope study of xenoliths from the Bartoy volcanoes. Contributions to Mineralogy and Petrology 111, 235–247.
Ionov, D.A., Harmer, R.E., 2002. Trace element distribution in calcite–dolomite carbonatites from Spitskop: inferences for differentiation of carbonatite magmas and the origin of carbonates in mantle xenoliths. Earth and Planetary Science Letters 198, 495–510.
Ionov, D.A., Blichert-toft, J., Weis, D., 2005. Hf isotope compositions and HREE variations in off-craton garnet and spinel peridotite xenoliths from Central Asia. Geochimica et Cosmochimica Acta 69, 2399–2418.
Ionov, D.A., Shirey, S.B., Weis, D., Brügmann, G., 2006. Os–Hf–Sr–Nd isotope and PGE systematics of spinel peridotite xenoliths from Tok, SE Siberian craton: effects of pervasive metasomatism in shallow refractory mantle. Earth and Planetary Science Letters 241, 47–64.
Jahn, B.M., Wu, F.Y., Chen, B., 2000. Massive granitoids generation in Central Asia: Nd isotope evidence and implication for continental growth in the Phanerozoic. Episodes 23, 82–92.
Jaques, A.L., Green, D.H., 1980. Anhydrous melting of peridotite at 0–15 kb pressure and the genesis of tholeiitic basalts. Contributions to Mineralogy and Petrology 73, 287–310.
Johnson, K.T.M., Dick, H.J.B., Shimizu, N., 1990. Melting in the oceanic upper mantle: an ion microprobe study of diopsides in abyssal peridotites. Journal of Geophysical Research 95, 2661–3267.
Johnson, K.T.M., 1998. Experimental determination of partition coefficients for rare earth and high-field-strength elements between clinopyroxene, garnet and basaltic melt at high pressures. Contributions to Mineralogy and Petrology 133, 60–68.
Kelemen, P.B., Whitehead, J.A., Aharonov, E., Jordahl, K.A., 1995. Experiments on flow focusing in soluble porous media with application to melt extraction from the mantle. Journal of Geophysical Research 100, 475–496.
Kempton, P.D., 1987. Mineralogic and geochemical evidence for differing styles of metasomatism in spinel lherzolite xenoliths: enriched mantle source regions of basalts? In: Menzies, M., Hawkesworth, C.J. (Eds.), Mantle Metasomatism. Academic Press, New York, pp. 45–89.
Klemme, S., van der Laan, S.R., Foley, S.F., Günther, D., 1995. Experimentally determined trace and minor element partitioning between clinopyroxene and carbonatite melt under upper mantle conditions. Earth and Planetary Science Letters 133, 439–448.
Li, X.H., Qi, C.S., Liu, Y., Liang, X.R., Tu, X.L., Xie, L.W., Yang, Y.H., 2005. Rapid separation of Hf from rock samples for isotope analysis by MC-ICPMS: a modified single-column extraction chromatography method. Geochimica 34 (2), 109–114.
Liu, J.Q., 1987. Chronology of Cenozoic Volcanic Rocks in Northeastern China. Acta Petrologica Sinica 4, 21–31 (in Chinese with English Abstract).
McArthur, J.M., 1994. Recent trends in strontium isotope stratography. Terra Nova 6, 331–358.
McKenzie, D.P., 1989. Some remarks on the movement of small melt fractions in the mantle. Earth and Planetary Science Letters 95, 53–72.
McDonough, W.F., McCulloch, M.T., 1987. The southeast Australian lithospheric mantle: isotopic and geochemical constraints on its growth and evolution. Earth and Planetary Science Letters 86, 327–340.
Mercier, J.C.C., Nicolas, A., 1975. Textures and fabrics of upper mantle peridotites as illustrated by xenoliths from basalts. Journal of Petrology 16, 454–487.
Menzies, M.A., Kempton, P.D., Dungan, M., 1985. Interaction of continental lithosphere and asthenosphere melts below the geronimo volcanic field, Arizona, USA. Journal of Petrology 26, 663–693.
Navon, O., Stolper, E., 1987. Geochemical consequence of melt percolation: the upper mantle as a chromatographic column. Journal of Petrology 95, 285–307.
Niu, Y.L., 1997. Mantle melting and melt extraction processes beneath ocean ridges: evidence from abyssal peridotites. Journal of Petrology 38, 1047–1074.
Nicolas, A., Lucazeau, F., Bayer, R., 1987. Peridotite xenoliths in Massif Central basalts: textual and geophysical evidence for asthenospheric diapirism. In: Nixon, P.H. (Ed.), Mantle Xenoliths. John Wiley, New York, pp. 563–574.
Norman, M.D., 1998. Melting and metasomatism in the continental lithosphere: laser ablation ICPMS analysis of minerals in spinel lherzolites from eastern Australia. Contribution to Mineralogy and Petrology 130, 240–255.
Nowell, G.M., Kempton, P.D., Noble, S.R., Fitton, J.G., Saunders, A.D., Mahoney, J.J., Taylor, R.N., 1998. High precision Hf isotope measurements of MORB and OIB by thermal ionization mass spectrometry: insights into the depleted mantle. Chemical Geology 149, 211–233.
Roden, M.F., Irving, A.J., Murthy, V.R., 1988. Isotopic and trace element composition of the upper mantle beneath a young continental rift: results from Kilbourne Hole, New Mexico. Geochimica et Cosmochimica Acta 52, 461–473.
Rudnick, R.L., Gao, S., Ling, W.L., Liu, Y.S., McDonough, W.F., 2004. Petrology and geochemistry of spinel peridotite xenoliths from Hannuoba and Qixia, North China craton. Lithos 77, 609–637.
Salters, V.J.M., Zindler, A., 1995. Extreme $^{176}Hf/^{177}Hf$ in the sub-oceanic mantle. Earth and Planetary Science Letters 129, 13–30.
Salters, V.J.M., Longhi, J., 1999. Trace element partitioning during the intial stages of melting beneath mid-ocean ridges. Earth and Planetary Science Letters 166, 15–30.
Schmidberger, S.S., Simonetti, A., Francis, D., Gariépy, C., 2002. Probing Archean lithosphere using the Lu–Hf isotope systematics of peridotite xenoliths from Somerset Island kimberlites, Canada. Earth and Planetary Science Letters 197, 245–259.
Simon, N.S.C., Carlson, R.W., Person, D.G., Davies, G.R., 2007. The origin and evolution of Kaapvaal Cratonic lithospheric mantle. Journal of Petrology 48, 589–625.
Song, Y., Frey, F.A., 1989. Geochemistry of peridotite xenoliths in basalt from Hannuoba, Eastern China: implications for subcontinental mantle heterogeneity. Geochimica et Cosmochimica Acta 53, 97–113.
Stosch, H.G., Seck, H.A., 1980. Geochemistry and mineralogy of two spinel peridotite suites from Dreiser Weiher, West Germany. Geochimica et Cosmochimica Acta 44, 457–470.
Stosch, H.G., Lugmair, G.W., 1986. Trace elements and Sr and Nd isotope geochemistry of peridotite xenoliths from the Eifel (W. Germany) and their bearing on the evolution of the subcontinental lithosphere? Earth and Planetary Science Letters 80, 281–298.
Stosch, H.G., Lugmair, G.W., Kovalenko, V.I., 1986. Spinel peridotite xenoliths from the Tariat Depression, Mongolia. II: geochemistry and Nd and Sr isotopic composition and their implication for the evolution of the sub-continental lithosphere. Geochimica et Cosmochimica Acta 50, 2601–2614.
Stracke, A., Bizimis, M., Salters, V.J.M., 2003. Recycling oceanic crust: quantitative constraints. Geochemistry, Geophysics, Geosystem, 4. doi:10.1029/2001GC000223.
Sweeney, R.J., Prozesky, V., Przybylowicz, W., 1995. Selected trace and minor element partitioning between peridotite minerals and carbonatite melts at 18–46 kb pressure. Geochimica et Cosmochimica Acta 59, 3671–3683.
Sun, S.S., McDonough, W.F., 1989. Chemical and isotopic systematics of oceanic basalts: implications for mantle composition and processes. In: Saunders, A.D., Norry, M.J. (Eds.), Magmatism in the Ocean Basins. Geological Society Special Publication, vol. 42, pp. 313–345.
Takazawa, E., Frey, F.A., Shimizu, N., Obata, M., 2000. Whole rock compositional variations in an upper mantle peridotite (Horoman, Hokkaido, Japan): are they consistent with a partial melting process? Geochimica et Cosmochimica Acta 64, 695–716.
Tanaka, T., Togashi, S., Kamioka, H., 2000. JNdi-1: a neodymium isotopic reference in consistency with LaJolla neodymium. Chemical Geology 168, 279–281.
Wang, L.C., 1996. Occurrence of the Dashihe olivine deposit in Jilin province, China. Journal of Changchun University of Earth Sciences 26, 43–46 (in Chinese with English abstract).
Wells, R.A., 1977. Pyroxene thermometry in simple and complex systems. Contribution to Mineralogy and Petrology 62, 129–139.
Witt-Eickschen, G., Seck, H.A., 1991. Solubility of Ca and Al in orthopyroxene from spinel peridotite: an improved version of an empirical geothermometer. Contribution to Mineralogy and Petrology 106, 431–439.
Wittig, N., Baker, J.A., Downes, H., 2007. U–Th–Pb and Lu–Hf isotopic constraints on the evolution of sub-continental lithospheric mantle, French Massif Central. Geochimica et Cosmochimica Acta 71, 1290–1331.
Wu, F.Y., Sun, D.Y., Li, H.M., Wang, X.L., 2001. The nature of basement beneath the Songliao Basin in NE China: geochemical and isotopic constraints. Physical Chemistry of Earth (A) 26, 793–803.
Wu, F.Y., Walker, R.J., Ren, X.W., Sun, D.Y., Zhou, X.Y., 2003. Osmium isotopic constraints on the age of lithospheric mantle beneath Northeastern China. Chemical Geology 196, 107–129.
Wu, F.Y., Walker, R.J., Yang, Y.H., Yuan, H.L., Yang, J.H., 2006. The chemical-temporal evolution of lithospheric mantle underlying the North China Craton. Geochimica et Cosmochimica Acta 70, 5013–5034.
Xu, Y.G., Menzies, M.A., Vroon, P., Mercier, J.C., Lin, C.Y., 1998a. Texture–temperature–geochemistry relationships in the upper mantle as revealed from Spinel Peridotite xenoliths from Wangqing, NE China. Journal of Petrology 39, 469–493.
Xu, Y.G., Menzies, M.A., Bodinier, J.L., Bedini, R.M., Vroon, P., Mercier, J.C., 1998b. Melt percolation–reaction atop the plume: evidence from poikiloblastic spinel harzburgite xenoliths from Boree (Massif Central, France). Contribution to Mineralogy and Petrology 132, 65–84.

Xu, Y.G., Sun, M., Yan, W., Liu, Y., Huang, X.L., Chen, X.M., 2002. Xenolith evidence for polybaric melting and stratification of the upper mantle beneath South China. Journal of Asian Earth Sciences 20, 937–954.

Xu, Y.G., 2002. Evidence for crustal components in mantle source and constraints on recycling mechanism: pyroxenite xenoliths from Hannuoba, North China. Chemical Geology 182, 301–322.

Xu, Y.G., Menzies, M.A., Thirlwall, M.F., Huang, X.L., Liu, Y., Chen, X.M., 2003. "Reactive" harzburgites from Huinan, NE China: products of the lithosphere–asthenosphere interaction during lithospheric thinning? Geochimica et Cosmochimica Acta 67, 487–505.

Xu, Y.G., Bodinier, J.L., 2004. Contrasting enrichments in high and low-temperature mantle xenoliths from Nushan, eastern China: Results of a single metasomatic eEvent during lithospheric accretion? Journal of Petrology 45, 321–341.

Xu, Y.G., Blusztajn, J., Ma, J.L., Suzuki, K., Liu, J.F., Hart, S.R., 2008. Late Archean to early Proterozoic lithospheric mantle beneath the western North China craton: Sr–Nd–Os isotopes of peridotite xenoliths from Yangyuan and Fansi. Lithos 102, 25–42.

Yaxley, G.M., Green, D.H., Kamenesky, V., 1998. Carbonatite metasomatism in the southeastern Australian lithosphere. Journal of Petrology 39, 1917–1930.

Yu, Y., 1987. Cenozoic Basalt from Qixingshan, Shuangliao, Jilin Province: its characteristic and origin study. Acta Petrologica Sinica 3, 55–62 (in Chinese with English abstract).

Yu, S.Y., Xu, Y.G., Huang, X.L., Ge, W.C., Cheng, J., 2007a. Comparison of composition and thermal state of the upper mantle beneath Northeast and North China: implications for lithospheric thinning in eastern China. Acta Petrologica Sinica 23, 1252–1268 (in Chinese with English abstract).

Yu, S.Y., Xu, Y.G., Huang, X.L., Ge, W.C., Ma, J.L., 2007b. Characteristics of melt-rock reaction in Shuangliao peridotite xenoliths and their implications to mantle metasomatism. Acta Petrologica et Mineralogica 26, 213–222 (in Chinese with English abstract).

Zhang, H.H., 2006. Geochemistry of Late Mesozoic–Cenozoic Basalts from Yitong-Datun and Shuangliao Area, Northeast China: Implication for Lithospheric Evolution and the Involvement of the Recycled Pacific Oceanic Crust in Basalt Genesis. Ph.D. Thesis, Graduate School of Chinese Academy of Sciences.

Zhao, X., Coe, R.T., Zhou, Y., Wu, H., Wang, J., 1990. New paleomagnetic results from Northern China: collision and suturing with Siberia and Kazakhstan. Tectonophysics 181, 43–81.

Zheng, J.P., O'Reilly, S.Y., Griffin, W.L., Lu, F.X., Zhang, M., Pearson, N.J., 2001. Relict refractory mantle beneath the eastern North China block: significance for lithosphere evolution. Lithos 57, 43–66.

Zheng, J.P., Griffin, W.L., O'Reilly, S.Y., Yang, J.S., Li, T.F., Zhang, M., Zhang, R.Y., Liou, J.G., 2006. Mineral chemistry of peridotites from Paleozoic, Mesozoic and Cenozoic lithosphere: constraints on mantle evolution beneath Eastern China. Journal of Petrology 47, 2233–2256.

Zhou, Q., Wu, F.Y., Chu, Z.Y., Yang, Y.H., Sun, D.Y., Ge, W.C., 2007. Sr–Nd–Hf–Os isotope characterizations of the Jiaohe peridotite xenoliths in Jilin province and constraints on the lithospheric mantle age in northeastern China. Acta Petrological Sinica 23, 1269–1280 (in Chinese with English abstract).

Zindler, A., Hart, S.R., 1986. Chemical geodynamics. Annual Review of Earth and Planetary Sciences 14, 493–571.